Palaeogeography, Palaeoclimatology, Palaeoecology 540 (2020) 109537

Contents lists available at ScienceDirect

Palaeogeography, Palaeoclimatology, Palaeoecology

journal homepage: www.elsevier.com/locate/palaeo

Globally enhanced Hg deposition and Hg isotopes in sections straddling the Permian–Triassic boundary: Link to volcanism

A.N. Sial[a,*], Jiubin Chen[b], L.D. Lacerda[c], C. Korte[d], J.E. Spangenberg[e], J.C. Silva-Tamayo[f], C. Gaucher[g], V.P. Ferreira[a], J.A. Barbosa[h], N.S. Pereira[i], A.P. Benigno[c]

[a] NEG–LABISE, Dept. of Geology, Federal Univ. of Pernambuco, Recife, PE 50740-530, Brazil
[b] Institute of Surface-Earth System Science, Tianjin University, 92 Weijin Road, 300072 Nankai, Tianjin, China
[c] LABOMAR, Institute of Marine Sciences, Federal Univ. of Ceará, Fortaleza 60165-081, Brazil
[d] Dept. of Geosciences and Natural Resource Management, University of Copenhagen, ØsterVoldgade 10, Copenhagen 1350, Denmark
[e] Institute of Earth Surface Dynamics (IDYST), University of Lausanne, CH-1015 Lausanne, Switzerland
[f] Faculty of Sciences, Antonio Nariño University, Circunvalar Campus, Bogota, Colombia
[g] Instituto de Ciencias Geológicas, Facultad de Ciencias, Universidad de la República, Montevideo, Uruguay
[h] Department of Geology, Federal University of Pernambuco, Recife 50740-530, Brazil
[i] Department of Biology, State University of Bahia, Campus VIII, Paulo Afonso, Brazil

ARTICLE INFO

Keywords:
C isotopes
Hg/TOC chemostratigraphy
Hg isotopes
Hg source
Permian–Triassic transition

ABSTRACT

Mercury (Hg/TOC) spikes from eight Permian–Triassic boundary (PTB) sections in this study display patterns similar to each other across the so-called extinction interval as well as strong variation in sedimentation rates from section to section. Mercury may have been originated from the synchronous magmatism of the Siberian Traps Large Igneous Province (STLIP).

At the GSSP in Meishan, China, Hg/TOC peaks were observed in the latest Permian mass extinction interval (LPME) and Early Triassic mass extinctions (ETME). The successions at Hovea-3 (Australia), Ursula Creek (Canada), Idrijca (Slovenia), Rizvanuša (Croatia) exhibit Hg/TOC peaks at the LPME and PTB. The Rizvanuša section displays one peak at the ETME horizon, Zal and Abadeh (Iran) successions at the LPME and ETME horizons, while Misci/Seres (Tyrol/Italy) section shows an enrichment at the LPME. The largest Hg/TOC peaks at the LPME, PTB and ETME are, perhaps, linked to the beginning of stage 2 (extrusive hiatus) of the Siberian Traps LIP. The meaning of the Hg/TOC spike between the LPME event and the PTB in seven of these sections is fuzzy.

In the δ^{202}Hg (MDF) vs Δ^{201}Hg (MIF) cross plot, the majority of samples from the extinction interval appear within the volcanic-emission box and a few samples plot in the sediment/soil/peat box. Hg-isotope signatures resulted from mixing processes of volcanic and normal marine sediment Hg, generating four horizontal trends whose Δ^{201}Hg shows negligible to no variation. Less terrigenous-Hg influx was noticed in the sections closer to the STLIP (Rizvanuša, Idrijca and Seres/Misci, all in Europe) in which Δ^{201}Hg (MIF) is close to zero. Marked influence occurs in sections far distant from the STLIP (Meishan, Ursula Creek and Hovea-3) that exhibit negative Δ^{201}Hg (MIF). The two sections from Iran, at intermediate distance from the STLIP, exhibit the highest, positive Δ^{201}Hg values (Abadeh section) and the lowest, negative Δ^{201}Hg values (Zal section). A Δ^{199}Hg (MIF) vs Hg (n·ng^{-1}) cross plot suggests that volcanic Hg has been contaminated by normal marine source-Hg influx in these sections helping to shape two major curved trends.

The negative C-isotope excursions and Hg/TOC enrichments in the studied sections are nearly coeval and this supports the hypothesis of synchronism between the Permian–Triassic transition biotic crises (LPME and ETME) and the start of the stage 2 of the Siberian Traps (sill-intrusion style of magmatism).

1. Introduction

Volcanic activity of large igneous provinces (LIPs) with millions of cubic kilometers emplaced in relatively short time intervals have been proposed as coeval with major mass extinctions during the Phanerozoic (Courtillot, 1994). A correlation between LIPs and mass extinction for

* Corresponding author.
E-mail address: sial@ufpe.br (A.N. Sial).

https://doi.org/10.1016/j.palaeo.2019.109537
Received 25 October 2019; Received in revised form 12 December 2019; Accepted 12 December 2019
Available online 16 December 2019
0031-0182/

the whole Phanerozoic Eon has been further suggested by several authors (e.g., Wignall, 2001; Courtillot et al., 1999; Courtillot and Renne, 2003; Kravchinsky, 2012; Bond and Wignall, 2014; Bond and Grasby, 2017).

There is a growing agreement that mercury (Hg) enrichment in sedimentary successions represents a potential indicator of massive volcanism effects allowing for a new insight into the relationship between LIP activity and periods of extreme environmental turnover (e.g., Sial et al., 2010, 2013, 2014, 2016, 2019; Nascimento-Silva et al., 2011, 2013; Sanei et al., 2012; Grasby et al., 2015a, 2017, 2019; Percival et al., 2015; Adatte et al., 2015; Font et al., 2016; Jones et al., 2017; Gong et al., 2017; Thibodeau et al., 2016; Thibodeau and Bergquist, 2017; Charbonnier et al., 2017; Sabatino et al., 2018; Burger et al., 2019; Meyer et al., 2019; Shen et al., 2019a,b,c; Them et al., 2019). As a result it has been raised the possibility that Hg enrichments across some chronological boundaries may represent true volcanogenic Hg loading to the environment, recorded by an increase in the ratio of Hg to total organic carbon (Hg/TOC) (e.g., Sanei et al., 2012; Grasby et al., 2013, Percival et al., 2015; references therein). Following this line of reasoning, search for Hg/TOC spikes across major chronostratigraphic boundaries has been expanded to cover the whole Phanerozic (e. g., Grasby et al., 2013, 2015b; Bond and Grasby, 2017; Gong et al., 2017; Jones et al., 2017; Percival et al., 2015, 2017, 2018; Burger et al., 2019; Korte et al., 2019; Shen et al., 2019a,b,c; Sial et al., 2016, 2019; Faggetter et al., 2019; Kwon et al., 2019; and references therein).

The demonstration of a link between the five major Phanerozoic mass extinctions known (Raup and Sepkoski, 1982) and LIP eruptions has defied researchers for decades. The most important challenges have been (a) the accurate dating of volcanic rocks produced by LIPs, and (b) of the sedimentary rocks which recorded abrupt biological and environmental changes leading to mass extinctions. In the current decade, contributions towards the refinement of LIPs radiometric dating (e.g., Burgess et al., 2014; Burgess and Bowring, 2015; Renne et al., 2015; Schoene et al., 2015, 2019; Sprain et al., 2019) and to Hg chemostratigraphy as a proxy for LIP activity in sedimentary successions rocks have received growing attention. However, less importance has been given to Hg isotopes as an additional key to demonstrate the volcanogenic origin of Hg enrichments across major chronological boundaries, except for a limited number of contributions (e.g., Sial et al., 2014, 2016, 2017, 2019; Thibodeau et al., 2016; Thibodeau and Bergquist, 2017; Grasby et al., 2017, 2019; Gong et al., 2017; Wang et al., 2018; Them et al., 2019; Shen et al., 2019a,b,c).

The variability in peak Hg values may be a consequence of different processes, as outlined for example by Percival et al. (2018): (a) range of atmospheric transport of Hg from the LIP source, (b) areas of higher primary productivity that may have greater Hg drawdown, (c) disturbance of local Hg reservoirs as a side effect of the LIP event, (d) subareal versus submarine eruptions, or (d) lithologic changes across an extinction boundary. Over 3500 Hg (Hg/TOC) analyses are available focusing on LIP eruptions versus major chronological boundaries, extinction events or OAEs, according to Grasby et al. (2019). However, some of the claimed Hg/TOC anomalies according to these authors are questionable, being unclear whether they represent truly a fingerprint of massive volcanism, or are just product of local/regional processes that generated an artifact.

In normalizing Hg, one should bear in mind that this metal is not only hosted by organic carbon, but can also be adsorbed onto clays (e.g., Sial et al., 2013) or hosted by sulfides under euxinic conditions (e.g., pyrite; Them et al., 2019; Shen et al., 2019d), increasing the complexity for the use of TOC to normalize Hg under reducing conditions.

2. Cause for massive extinction in the Permian–Triassic transition

The Permian–Triassic extinction event is known as the P–Tr extinction, the P–T extinction, End-Permian Mass Extinction (EPME), latest Permian Mass extinction (LPME) and, colloquially, as the Great Dying. It was the most severe mass extinction in the Earth history with devastating impact on both terrestrial and marine ecosystems (e.g., Benton, 2003; Erwin, 2006; Erwin et al., 2002; Algeo et al., 2007; Chen and Benton, 2012). There is evidence for one (Jin et al., 2000; Rampino et al., 2000; Shen et al., 2011; Wang et al., 2014; Burgess et al., 2014) to three distinct pulses (or phases) of extinction in the Permian–Triassic transition (e.g., Yin et al., 1992, 2001; Sahney and Benton, 2008; Song et al., 2009, 2013). Two phases of ecosystem perturbations were also evidenced by biomarkers (Xie et al., 2005) and reducing conditions (Shen et al., 2016). The latest Permian mass extinction (LPME) was associated with major environmental perturbations over a short time interval and there are still questions about the exact patterns and timing of the extinction (e.g., Shen and Bowring, 2014). Potential causes for those extinction pulses include massive volcanic eruptions such as the Siberian Traps, known as one of the two most voluminous continental volcanic eruptions on Earth (Coffin and Gahagan, 1995) and related greenhouse gas emissions (e.g., Ogdena and Sleep, 2011; Brand et al., 2012, 2016; Burgess et al., 2017, and several others), climate change brought on by large releases of underwater methane or methane-producing microbes (Chandler, 2014) and one or more large meteor impact events (see Erwin, 2003, for a critical evaluation). The connection between the Siberian Traps LIP (STLIP) magmatism and the Permian–-Triassic extinction is supported by a striking temporal coincidence between the two phenomena (Burgess and Bowring, 2015; Burgess et al., 2014). According to Burgess and Bowring (2015), STLIP magmatism started at about 300,000 years prior to the LPME and lasted 800,000 years. Calcium and boron isotopes have suggested ocean acidification triggered by STLIP across the LPME (Payne et al., 2010; Clarkson et al., 2015). Although it seems clear that this flood basalt volcanism has influenced marine ecosystems (Chen and Benton, 2012), and induced denudation of terrestrial plants and wildfires (Benton and Newell, 2014), the exact cause of the LPME extinction is still unknown. Possibly, Hg had a widespread toxic impact as Hg emission rates from the STLIP reached levels of about 32%–399% above modern geogenic sources (Grasby et al., 2017) which are estimated to be 0.8–10 Gg/yr. The biotic crisis was accompanied by a widespread episode of oceanic photic zone euxinia, perhaps lasting for about 10 M.y., as a 'superanoxic event' (e.g. Isozaki, 1997; Grice et al., 2005), also regarded as a potential kill mechanism (e.g., Wignall and Twitchett, 1996, 2002).When the Permian–Triassic extinction event is compared with the end-Triassic and end-Cretaceous mass extinctions, one sees in common; (a) a short-lived perturbation of the carbon cycle followed by rise of atmospheric pCO_2 and temperature, (b) evidence for ocean acidification, (c) anoxia, and (d) rapid extinction rates (e.g., Burgess et al., 2014).

An asteroid impact could be potentially a further kill mechanism for the latest Permian massive extinction scenario, as the abrupt isotopic and faunal boundary ($\sim 10^4$ yr; Shen et al., 2011) is evocative of a major bolide impact (Erwin, 2003; Tohver et al., 2017). A possible bolide impact at the Permian–Triassic boundary has been so far preferentially sought on the Tethyan realm (e.g., Retallack et al., 1998; Basu et al., 2003; Koeberl et al., 2004). Retallack et al. (1998) have investigated this hypothesis by examining chemical and mineralogical behaviors of shocked quartz and iridium in PTB sections at Graphite Peak and Mount Cream, Antarctica, and Wybung Head in Australia. Results of their investigation failed to support bolide impact as one of the main causes of the huge extinction in the Permian–Triassic transition at least in the examined localities. Becker et al. (2004) has examined the P–T boundary breccia cored at a depth of 3044 m at the Bedout-1 well, western Australia, as possible end-Permian impact crater. An age of 250.7 ± 4.3 Ma ($^{40}Ar/^{39}Ar$ dating in plagioclase) has been obtained, within the experimental error from the age of the Permian–Triassic extinction event (251.4 ± 0.4 Ma) and Siberian Norilsk volcanism (251.7 ± 0.4 to 251.1 ± 0.3 Ma. However, this stimulating finding lacks further support to confirm Bedout as an asteroid impact crater as no impact effects have been so far identified (Glikson, 2004). The

40 km-wide Araguainha impact event (Lana et al., 2008) in the intracratonic Parana Basin of Brazil may represent another record of asteroid impact at about the Permian–Triassic transition. Tohver et al. (2017) demonstrated that this catastrophic event created one of the world's most extensive seismite-tsunamite couplets in the latest Permian (254.7 ± 2.5 Ma) and that the geographic radius affected by this impact event approached continental scale.

3. Study aims and selected Permian–Triassic sections

The present study aims at: (a) searching for Hg spikes (Hg/TOC) in eight marine sediments in sections straddling the Permian–Triassic transition to investigate the global extent of Hg loading to the environment, related to STLIP magmatic activities, (b) examining Hg isotopes to assess if the Hg and the Hg/TOC spikes within the mass extinction interval are volcanogenic and may serve as fingerprints of the STLIP magmatic activities and (c) contrasting Hg isotope signatures in Permian–Triassic sections to K/Pg boundary ones elsewhere, regarded as fingerprints of Deccan eruptions, and (d) from Hg/TOC stratigraphic patterns, we hope to broaden the knowledge of worldwide fingerprints of the stages of the STLIP magmatic activities.

In selecting sections in this study, eight well-known Permian–Triassic marine sections, widely separated, from different paleolatitudinal zones, most of them regarded as near-complete ones, have been chosen (Fig. 1): (a) Ursula Creek in Canada (55° 59′ 43″ N; 123° 9′ 54″W, (b) Meishan (GSSP) in China (31° 5′ 39″N; 119° 41′ 24″E), (c) Misci in Italy (46° 38′ 23″N; 11° 50′ 35″E), (d) Rizvanuša in Croatia (44° 29′ 56″N; 15° 18′ 8″E) (Fig. 2), (e) Zal and Abadeh in Iran (38°39′ 1″N; 45° 51′ 59″E), (f) Idrijca in Slovenia (46° 5′ 19″N; 13° 53′ 26″E) and (g) Hovea-3 in Australia (29° 19′ 9.17″S; 115° 2′ 23.29″ E) (Fig. 3). For most of these sections, previous studies had applied high-resolution biostratigraphy and environmental multi-proxies such as: (1) organic and inorganic carbon isotope stratigraphy, (2) sedimentology and micro-facies analysis, (3) major and trace element geochemistry. Examining marine sections, thousands of kilometers apart, from different margins of paleo-oceans—Panthalassa (Ursula Creek), western margin of Paleotethys (Seres/Misci, Idrijca, Rizvanuša, Zal and Abadeh), eastern margin of Paleotethys (Meishan) and Neotethys margins (Hovea-3)—increase the possibility of telling apart local from global fingerprints in these sections.

3.1. Ursula Creek succession, Canada

A few kilometers west of the mouth of the Ursula Creek, on the shores of the Lake Williston, British Columbia, Canada, there is a near-vertically dipping, continuous Middle Permian to Middle Triassic section whose stratigraphic record has been studied by Wignall and Newton (2003). In this section, chert beds of the Fantasque Formation and the overlying shales of the Grayling and Toad formations record the Permian–Triassic transition according to these authors. The location of this transition in this section was based on a negative spike of $\delta^{13}C_{org}$ (Wang et al., 1994), and later confirmed by conodont evidence by Wignall and Newton (2003) who regarded this section as an Upper Permian to Lower Triassic deep-water record at the Pangea margin. They compared this to another PTB section at Selong, South Tibet, located at high paleolatitude of the southern margin of the Neotethyan Ocean and concluded that the LPME was diachronous by half a million years or more, with late Changxingian extinction recognized in Panthalassa.

3.2. Seres/Misci (Tyrol), Rizvanuša (Croatia), Idrijca (Slovenia) successions

The samples from the Misci succession analyzed in this report were collected by Kraus et al. (2013) from a Permian–Triassic section at Misci described by Bosellini (1964), a locality also named “Val Badia” in Sephton et al. (2002) or “Val Seres” (Cirilli et al., 1998), at the Dolomites in the Southern Alps, South Tyrol. This section is exposed about 600 m west-northwest of the Misci settlement, north of the Rio Seres (Cirilli et al., 1998) and the studied profile (46°38″ 23′N; 11°50″35′ E) comprises the upper part of the Bellerophon Formation and the lower part of the Werfen Formation, the latter consisting of the Tesero Oolite Horizon (oolitic grainstones) and the lower Mazzin Member.

The Bellerophon Formation, base of this section, is composed of thick-bedded wackestone and mudstone, alternating with beds of thin platy marls. The Bulla Member consists of dolomitic mudstone, interbedded with packstone and marl while the Mazzin Member consists of mudstone interbedded with thin-bedded marl. Sedimentological observations and palaeogeographical reconstruction indicate shallower-water depths towards the west of this basin (Brandner et al., 2009; Kraus et al., 2013).

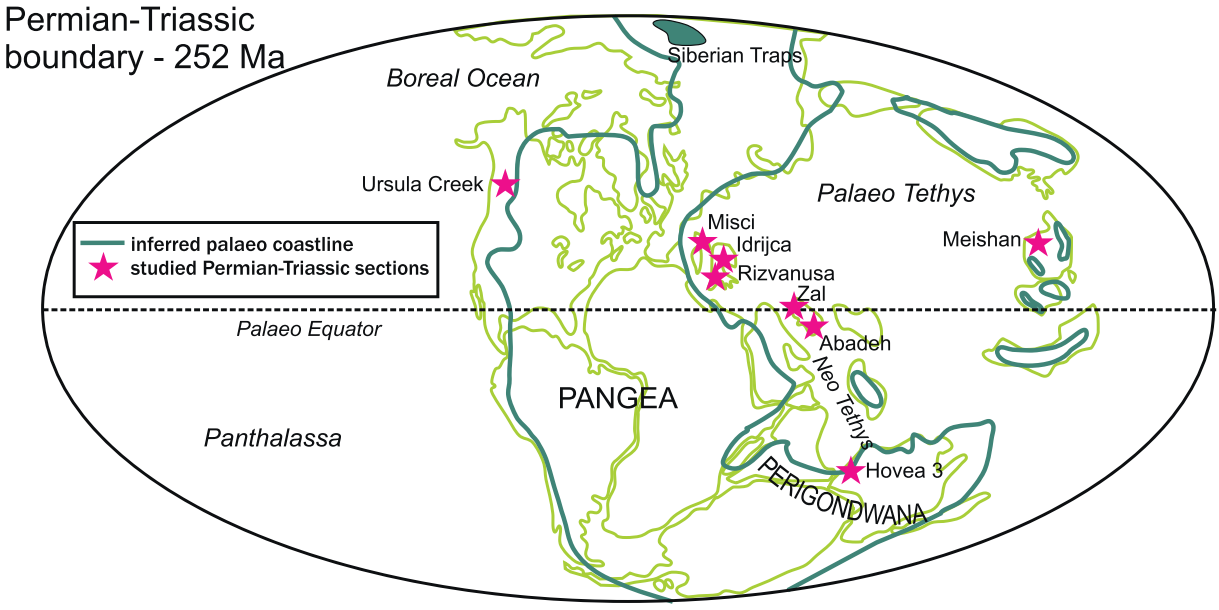

Fig. 1. Global palaeogeographical reconstruction during the Permian–Triassic transition (modified from Wignall and Twitchett, 2002; Thomas et al., 2004) and global geographical distribution of the Permian–Triassic sections in this study.

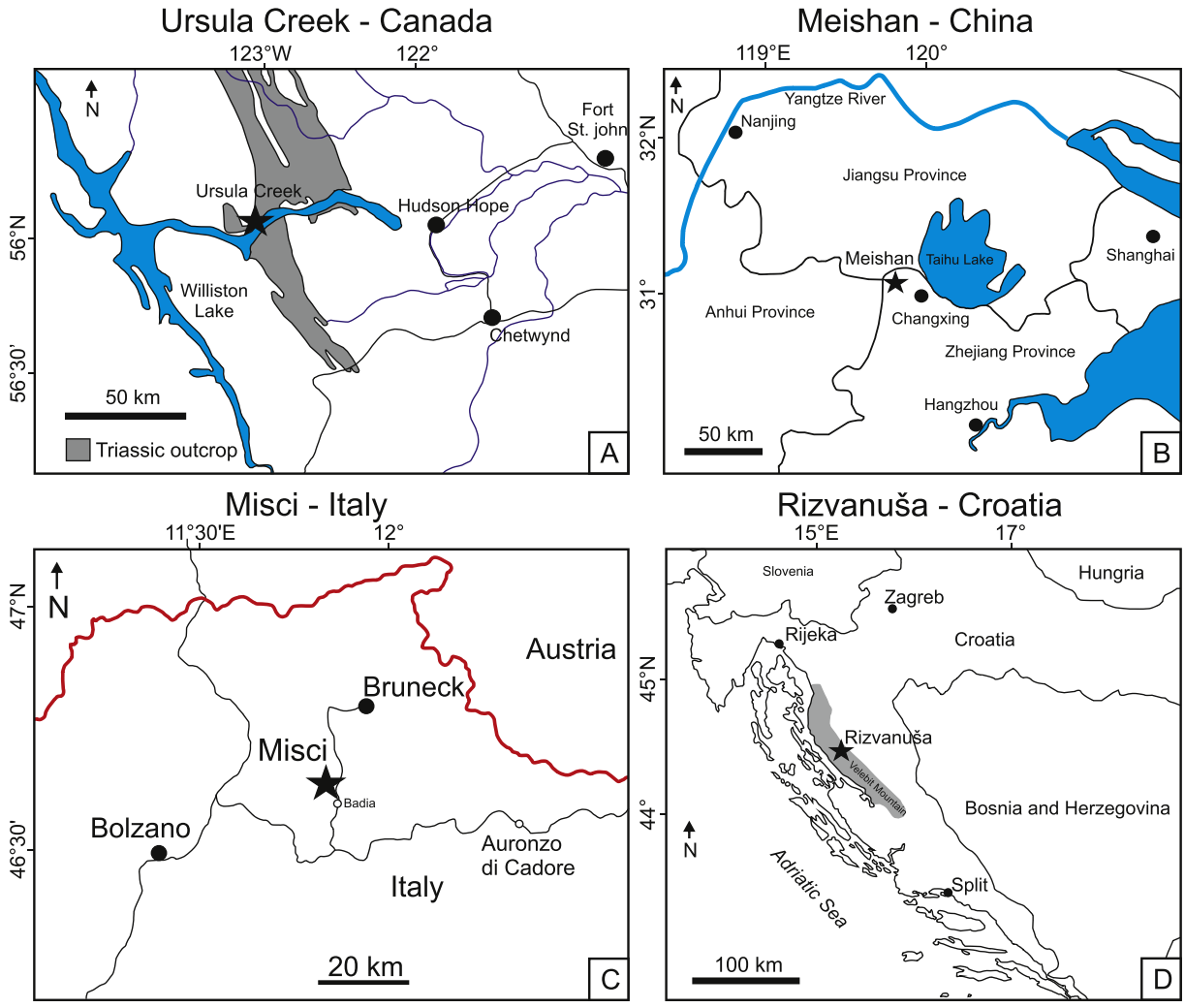

Fig. 2. Geographical sketch maps showing localities of four sections in this study: (a) Ursula Creek, Canada (after Wignall and Newton, 2003); (b) Meishan, China (based on Li and Jones, 2017); (c) Seres/Misci, southern Alps, modified from Kraus et al. (2013); (d) Rizvanuša, Croatia, modified from Fio et al. (2010).

In Croatia, Fio et al. (2010) have used stable isotopes, rare-earth elements and trace element geochemistry of marine carbonate rocks from two continuous sections in the Velebit Mountain, to investigate the position of the Permian–Triassic boundary. These two sections, Rizvanuša and Brezimenjača, comprise two lithostratigraphic units: (a) Upper Permian Transitional Dolomite and (b) overlying Sandy Dolomite. The chronostratigraphic Permian–Triassic boundary was for sometime regarded to be located at the contact between these two units that is characterized by occurrence of ooids, siliciclastic grains and erosional features (Fio et al., 2010).

An assemblage of Permian fossils was found in the Rizvanuša section, in the Sandy Dolomite unit about 5 m above this contact, comprising *Geinitzina*, *Globivalvulina*, *Hemigordius*, bioclasts of gastropods, ostracods and brachiopods (Fio et al., 2010, 2013). A negative $\delta^{13}C$ excursion was observed within the lower part of the sandy dolomite unit in both sections, Rizvanuša and Brezimenjača, and this level has been proposed by these authors as the chemostratigraphic Permian–-Triassic boundary.

At the Idrijca Valley, about 20 km West of Ljubljana in the Carnic Alps of western Slovenia, Permian–Triassic marine carbonate rocks were deposited in a forearc basin setting in the northeastern Paleotethys (Baud et al., 1989; Stampfli et al., 2001). Preliminary sedimentological and paleontological studies of these nonmetamorphosed carbonate rocks were carried out by Ramovs (1986) and Dolenec et al. (2001).

The uppermost portion of the 250 m thick Zazar Formation has recorded the Upper Permian at the Idrijca Valley and is composed of black, abundantly fossiliferous, shallow-marine carbonate rocks. Dark-gray and black limestone layers interbedded with rare black shale constitute the 5–40 cm upper part of this formation (Ramovs, 1986). Towards the Permian–Triassic boundary, a gradual impoverishment is experienced by the faunal composition, with abrupt disappearance at the boundary (Dolenec et al., 2001). The Permian–Triassic boundary is marked by a 0.8 cm thick clayey marl layer whose deposition likely took place during a period of maximum eustatic sea-level fall. According to Dolenec et al. (1999) it is overlain by a light-gray well-bedded Lower Scythian Formation comprising sparitic, dedolomitized limestone. The faunal disappearance at the Permian–Triassic boundary is accompanied by negative $\delta^{13}C_{carb}$ and $\delta^{13}C_{org}$ excursions and a strong pulse of magnetic susceptibility (Dolenec et al., 2001).

3.3. Zal and Abadeh successions, Iran

Two Permian–Triassic sections in Iran were targeted of attention in this study, Zal and Abadeh, located at the same margin of the Neotethys Ocean. High-resolution chemostratigraphy, available for both sections, has been tested for isochrony on the basis of an updated high-resolution conodont and ammonoid biostratigraphy (Kozur, 2007; Richoz et al., 2010; Ghaderi et al., 2014).

Carbonate rocks for the Permian–Triassic boundary section at Zal, NW-Iran, were deposited in an open-marine, pelagic environment.

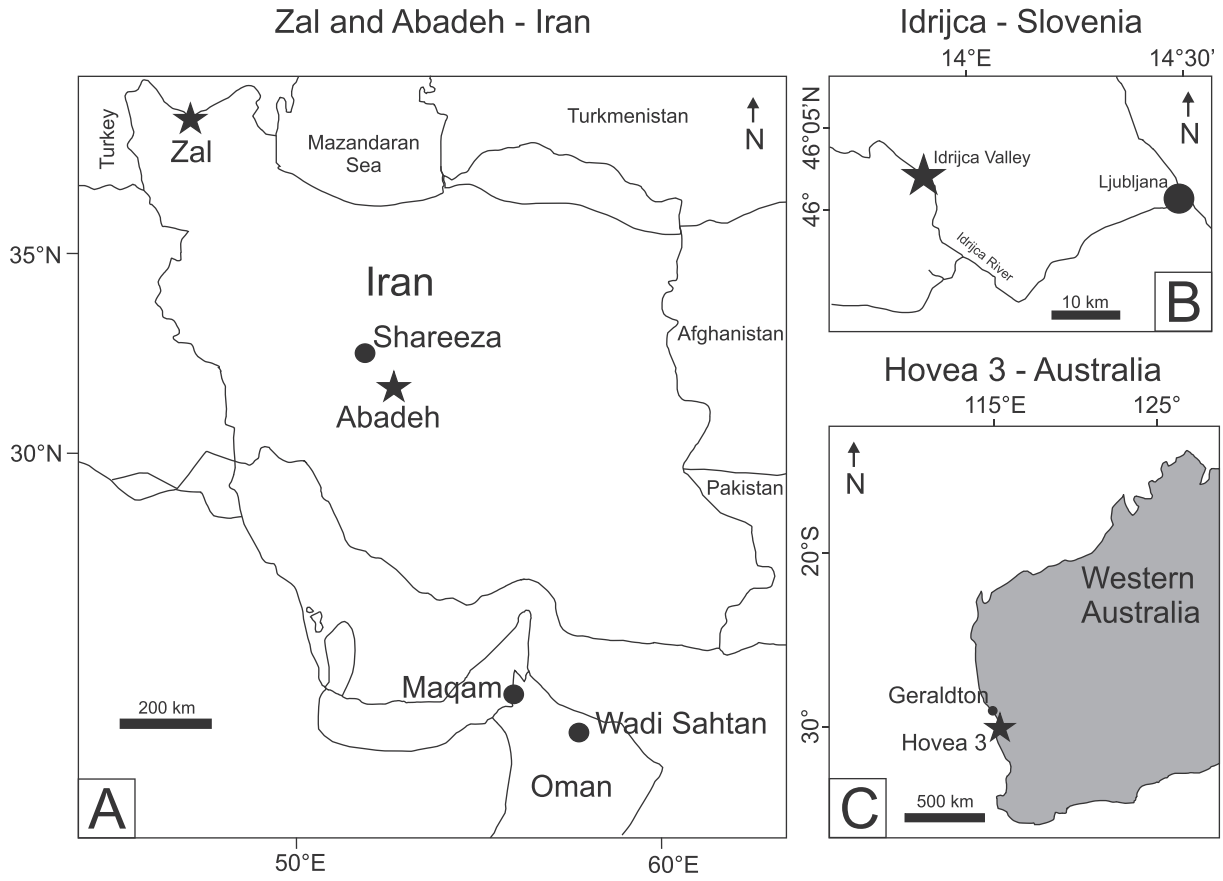

Fig. 3. Geographical localities of the other four sections: (a) Zal and Abadeh (central Iran, Middle East) sections, modified from Richoz et al. (2010); (b) Idrijca, western Slovenia, based on Schwab and Spangenberg (2004) and (c) Hovea-3, western Australia (based on Thomas et al., 2004).

Because of a greater water depth compared to other Iranian Permian–Triassic sections, the *C. meishanensis-H. praeparvus* Zone and the *H. parvus* Zone are also rich in conodonts and the stratigraphy is thus well constrained (Korte et al., 2004a). The completeness of the Zal PTB-succession is attested by the presence of all Dzhulfian, Dorashamian and the lowermost Triassic (*H. parvus*) conodont Zones (Korte et al., 2004b, 2010). Lithologic succession, detailed C-isotope stratigraphy and biostratigraphy have been summarized in Korte et al. (2010).

Pelagic deposits at Abadeh whose sedimentation presumably happened at water depth between 60 and 90 m, represent a complete biostratigraphic record across the Permian–Triassic boundary. Detailed chemostratigraphic (C, O, S, Sr isotopes) and biostratigraphic studies were carried out by Korte et al. (2004c, 2010). The Abadeh succession was deposited on the northern shelf of the Neotethyan Ocean (Stampfli and Borel, 2002), or, more precisely, at the southern margin of the Sanandaj-Sirjan block, a part of the Cimmerian microcontinent. The stratigraphy at the Abadeh section is based mostly on conodonts and summarized in Kozur et al. (1975, 1978), Kozur and Weems, (2010) and Taraz et al. (1981).

Although abundant palaeontological, biostratigraphical, and geochemical data, from the Upper Permian to Lower Triassic, at the Abadeh section are available, the precise positions of the Permian–Triassic (PTB), Guadalupian–Lopingian (LGB) and Wuchiapingian–Changihsingian (WCB) boundaries are still debated in view of different fossil groups and different taxonomic approaches (Liu et al., 2013).

3.4. Meishan succession (GSSP), China

One of the most used data sets in the search for unravelling the extinction at the latest Permian is from the Global Stratotype Section and Point (GSSP) of the Permian-Triassic boundary at the Meishan section, South China (Fig. 8). The extinction interval corresponding to Beds 25–28 at Meishan, shown in this figure, is of only 0.36 m and may contain several depositional hiatuses at or below the Permian–Triassic boundary (Cao and Zheng, 2007, 2009; Zheng et al., 2013; Shen et al., 2018). This extinction interval corresponds to a maximum of 61 ± 48 kyr, according to Burgess and Bowring (2015). The U—Pb dates on Siberian Traps LIP lava flows, sills, and explosively erupted rocks carried out by these authors demonstrate that (a) about two-thirds of the total lava/pyroclastic volume was erupted over around 300 kyr, before and concurrent with the LPME; (b) eruption of the balance of lavas continued for at least 500 ky after the cessation of the extinction; and (c) massive emplacement of sills into shallow crust began concomitant with the mass extinction and continued for at least 500 ky into the early Triassic. This age calibration from Burgess and Bowring (2015) coupled with statistical analyses of fossil evidence point to a single, brief catastrophic latest Permian extinction supporting previous assumptions by Jin et al. (2000), Rampino et al. (2000), Shen et al. (2011) and Wang et al. (2014). It further demonstrated a robust synchronism between LPME and Siberian Traps magmatism with lava and pyroclastic eruptions predating the onset of extinction by 300 ± 126 ky.

3.5. Hovea-3 (petroleum borehole), Perth Basin, Australia

The Permian–Triassic Hovea-3 is the first marine Permian–Triassic boundary documented in Australia. Located at the Perth Basin of Western Australia (29° 19′ 9.17″S, 115° 2′ 23.29″E) this petroleum borehole was continuously cored from 1968.5 m to 2049.85 m, and it has been studied in detail by Thomas et al. (2004). The Hovea Member, a distinctive zone, is 27.7 m thick in Hovea 3 and it is enriched in

organic matter at the base of the marine Kockatea Shale (Thomas and Barber, 2004).This shale forms the impermeable cap rock for the Dongara Sandstone, which was deposited in a foreshore–shoreface environment.

The age control for the Hovea 3 core was based on palynology and macrofossils (brachiopods and bivalves).According to Thomas et al. (2004), conodonts have not been recovered from this succession yet, likely because of the limited amount of rock material available, and scarcity of this fossil group in Gondwanan sections that was ascribed to high palaeolatitude (Archbold, 2000). The lower inertinitic interval (presence of oxidized organic material or fossilized charcoal) of the Hovea Member is composed of fossiliferous black mudstone, sandy siltstone and shelly storm beds, deposited in shallow-marine environment during the earliest stage of a marine transgression (Thomas et al., 2004). These environments were likely well-oxygenated ones judging from their variably bioturbated nature.

Biomarkers diagnostic of anoxygenic photosynthesis by Chlorobiaceae are particularly abundant at the Permian–Triassic boundary and into the Early Triassic (Grice et al., 2005). This demonstrates that waters of the Tethys Ocean were periodically euxinic in the photic zone during and right after the latest Permian extinction event.

4. Analytical methods

4.1. Analysis of C isotopes and total organic carbon (TOC)

Stable carbon isotope analyses ($\delta^{13}C_{carb}$) of carbonate rock samples from Idrijca and Rizvanuša sections were performed using a Thermo Fisher Scientific (Bremen, Germany) Gas Bench II carbonate preparation device connected to a Delta Plus XL isotope ratio mass spectrometer at the University of Lausane, Switzerland. The CO_2 extraction was done by reaction with anhydrous phosphoric acid at 70 °C for calcite and at 90 °C for dolomite. The stable carbon isotope ratios are reported in the delta (δ) notation as the permil (‰) deviation relative to the Vienna Pee Dee belemnite standard (VPDB). The standardization of the $\delta^{13}C_{carb}$ values relative to the international VPDB scale was done by calibration of the reference gases and working standards with international reference materials NBS 18 (carbonatite, $\delta^{13}C = -5.04$‰) and NBS 19 (limestone, $\delta^{13}C = +1.95$‰). Analytical uncertainty (1 sigma), monitored by replicate analyses of the international calcite standard NBS19 and the laboratory standards Carrara Marble ($\delta^{13}C = +2.05$‰) was not greater than ± 0.05‰ for $\delta^{13}C_{carb.}$.

The carbon isotope composition of organic matter ($\delta^{13}C_{org}$) in the decarbonated fraction (HCl treatment) was determined by flash combustion on a Carlo Erba 1108 elemental analyzer connected to a Thermo Fisher Scientific Delta V Plus isotope ratio mass spectrometer that was operated in the continuous helium flow mode via a Conflo III split interface. The repeatability and intermediate precision of the $\delta^{13}C_{org}$ analyses, determined by the standard deviation of replicated analyses of laboratory organic standards and unknown samples, were better than 0.1‰ (1 SD). The accuracy of the analyses was checked periodically by analyses of the international reference materials (USGS-24 graphite, IAEA-PEF1 polyethylene foil, and NBS-22 oil). The total organic carbon (TOC in wt%) content was determined from total peak area obtained from the EA/IRMS measurements—and corrected for the weight by acidification—, and/or by Rock-Eval 6 pyrolisis of the whole-rock sample. Samples from Abadeh, Seres/Misci, Meishan and Zal sections were decarbonated using 6 M HCl prior to TOC analyses at the IGN, University of Copenhagen. Acid remains were subsequently removed by a repeated procedure of rinsing, centrifugation, and decantation of supernatant liquids. Remaining fractions were weighed out again after 24 h freeze drying at temperatures of −54 °C. $CaCO_3$ concentration was calculated by the weight difference of the aliquots before and after the acid treatment. The total organic carbon was measured on 160 mg of decarbonated aliquot using a Carbon-Sulphur-Determinator (Eltra CS 500). The sample was combusted for 90 s in a ceramic boat at a temperature of ~1350 °C with a catalytic oxidation process. Resulted CO_2 signal was electronically linearized and integrated, and subsequently used to calculate the TOC. The reproducibility, obtained from multiple analyses of the in-house reference material SKK-9 (TOC = 6.88%), is generally better than 0.1% (1 sd). Samples from Meishan were measured for $\delta^{13}C_{org}$ at the University of Copenhagen by using an EA Elemental Analyzer coupled with the Isoprime isotope ratio mass spectrometer. Weight dependent isotope fraction was corrected by a polynomial fit (r = 0.95) of at least 15 in house reference samples covering the entire weight range of the samples. The reproducibility of the data was better than 0.2‰ (2 sd).

Aliquots (400 to 1000 μg) of Meishan bulk rock carbonate powders were reacted at 70 °C in sealed glass vials (~50 μL) with manually added anhydrous phosphoric acid after removing atmospheric gases. Generated carbon dioxide was analyzed for $\delta^{13}C$ and $\delta^{18}O$ with an IsoPrime triple collector Isotope Ratio Mass Spectrometer at the Department of Geosciences and Natural Resource Management, University of Copenhagen. Weight-dependent isotope fractionation was corrected by using calibration curves constructed from analyses of the in-house standard LEO (Carrara Marble; $\delta^{13}C = +1.96$‰ V-PDB; $\delta^{18}O = -1.93$‰ V-PDB). The analytical precision (2sd) of the analyses calculated from repeated measurements of LEO was better than 0.1‰ for $\delta^{13}C$ and better than 0.2‰ for $\delta^{18}O$.

Organic carbon isotope measurements for the Zal section were operated at the GeoZentrum Nordbayern, University of Erlangen-Nürnberg, using the Flash EA 2000 elemental analyzer connected to a ThermoFinnigan Delta V Plus mass spectrometer. The results are reported in the δ-notation in permil relative to the V-PDB standard. The accuracy and reproducibility of the data were controlled by replicate analyses of the Erlangen laboratory standard (−27.32‰) calibrated to international standards USGS 40 and 41. The reproducibility was ± 0.1‰ (1σ). For the Seres/Misci and Abadeh sections, $\delta^{13}C_{org}$ measurements from Kraus et al. (2013) and Korte et al. (2004c), respectively, have been used.

The $\delta^{13}C_{org}$ measurements for Ursula Creek section used in this study are from Wang et al. (1994) and for the Hovea-3 section are from Thomas et al. (2004). TOC analyses of samples from the Hovea-3 and Ursula Creek sections, analyzed by Rock-Eval 6 pyrolisis of whole-rock samples, are also found in those two studies.

4.2. Analysis of mercury

Mercury concentrations of all samples in this study were determined in homogenized powdered samples. Glass and plastic wares were decontaminated by immersion for 1 day in (10% v/v) Extran solution (MERCK), followed by immersion for 1 day in diluted HCl (5% v/v) and final rinsing with Milli-Q water. All chemical reagents used were at least of analytical grade. Cold Vapor Atomic Fluorescence Spectrophotometry, equipped with a Millenium Merlin PSA spectrophotometer, was used for Hg determination, after Hg^{2+} reduction with $SnCl_2$ All samples were analyzed in duplicates, showing reproducibility within 9.5%. A certified reference material (NIST 1646a, Sigma Aldrich) was simultaneously analyzed to evaluate Hg determination accuracy. Such analysis showed a precision of 4%, as indicated by the relative standard deviation of three replicates, and presented Hg recovery varying from 79% to 96% (average 89%). Sample duplicates differ in < 5%. The Hg detection limit estimated as 3 times the standard deviation of reagent blanks, was 0.02 $ng{\cdot}g^{-1}$. In all cases, blank signals were lower than 0.5% of sample analysis. Concentration values were not corrected for the recoveries found in the certified material.

4.3. Analysis of mercury isotopes

Mercury isotope ratios of all samples in this study were determined on the new MC-ICP-MS (Nu-Plasma, Nu Instruments) at the Institute of Surface-Earth System Science of Tianjin University, China, following a

method similar to Huang et al. (2015). A homemade continuous flow cold-vapor generation system (CV) was coupled with an Aridus II desolvation unit (CETAC Technologies, U.S.) for Hg and Tl introduction, respectively. The instrumental baseline was measured by defocusing before each sample and standard. Both the internal standard method and the standard-sample bracketing technique were used to correct for instrumental mass bias (Chen et al., 2010; Jiskra et al., 2012).

Mass-dependent fractionation (MDF) of Hg isotopes is reported in delta notation, δ, which is the permil (‰) deviation relative to the SRM 3133 standard. Mass-independent fractionation (MIF) of Hg isotopes is reported using upper-case delta notation, Δ, which is the deviation of the measured isotope ratio from the theoretical ratio predicted by MDF. The analytical quality was controlled by repeated measurement of standard materials. Long-term analysis gave average values of −0.54 ± 0.10‰, −0.02 ± 0.04‰ and −0.04 ± 0.04‰ for δ^{202}Hg, Δ^{199}Hg and Δ^{201}Hg of UM-Almaden Hg (2SD, n = 21), and of −1.22 ± 0.16‰, 0.06 ± 0.09‰ and 0.03 ± 0.10‰ for those of Fluka Hg (2SD, n = 13), respectively, in accordance with the published results (Bergquist and Blum, 2007; Blum and Bergquist, 2007; Chen et al., 2010; Chen et al., 2012; Jiskra et al., 2012). The 2SD of the isotopic compositions of the UM-Almaden were considered as the analytical uncertainty for the isotopic compositions of samples. When the uncertainty of the replicate isotopic measurements of one sample was larger than the 2SD of the UM-Almaden, the uncertainty was applied to the sample.

5. Results and discussion

5.1. Hg and Hg/TOC chemostratigraphy

The behavior of $\delta^{13}C_{carb}$ and $\delta^{13}C_{org}$ pathways of bulk sedimentary rocks across the Permian–Triassic transition was discussed in detail by Korte and Kozur (2010). This transition is marked by distinct perturbations in the global carbon cycle resulting in a marked negative $\delta^{13}C$ excursion at the Permian–Triassic boundary, well known from many marine and continental sedimentary successions. Because of the well-calibrated conodont biostratigraphy (e.g., Wang and Wang, 1981; Mei et al., 1998; Kozur, 2004, 2005, 2007), it is possible to have a good control on the long-term C-isotope trend across the Permian–Triassic boundary in sections like Meishan in China (e.g., Cao et al., 2002) or Shahreza in Central Iran (Korte et al., 2004b).

The burial and re-oxidation of ^{13}C-depleted organic matter in the oceans or on continents seem to control the carbon-isotope ratio of the ocean/atmosphere (Scholle and Arthur, 1980; Kump and Arthur, 1999). However, some additional causes have led to negative $\delta^{13}C$excursions around the P–T boundary. Among them, Korte and Kozur (2010) have listed the influence of the STLIP and contemporaneous volcanism by (a) exhalation of ^{13}C-depleted CO_2, (b) destabilization of methane from permafrost soils and/or pre-Trap coals, or (c) thermal metamorphism of pre-Trap organic-rich sediments. If these are potential causes, Hg that is an important fingerprint for volcanism would be expected to exhibit a positive Hg/TOC spike whenever an import $\delta^{13}C$ drop is recorded, if volcanism has played a direct or indirect role in shaping the $\delta^{13}C$ pathway.

In the present study, Hg and TOC were analyzed in samples from all eight sections under consideration and results are shown in Table 1 and their chemostratigraphic curves have been plotted in Figs. 4 through 7 and 9 through 11, alongside $\delta^{13}C_{carb}$ and/or $\delta^{13}C_{org}$ curves. Before examining the Hg and Hg/TOC results obtained in this study, it is convenient to consider a few points brought up by Grasby et al. (2019) on the use of TOC data in normalization of Hg values. As pointed out by these authors, extremely low TOC values (< 0.2 wt%) are likely unreliable for even the most accurate methods of TOC determination and, therefore, they cautioned the use of TOC values that are < ~0.5 wt%. By examining TOC values reported in the literature (around 2500) they observed that only 75% of them were larger than 0.2 wt% implying that about 25% of reported Hg/TOC values are spurious.

Among the sections examined in this study, only the Hovea-3 section exhibits all samples with TOC values > 0.20 wt%. About 70% of the samples from the Ursula Creek section yielded TOC values > 0.20 wt% and only 30% of the Meishan samples. In the other sections (Seres/Misci, Idrijca, Rizvanuša, Zal, Abadeh) TOC values are < 0.20 wt% with few exceptions. This picture discourages the use of TOC to normalize the Hg values in this study as it would potentially lead to generate questionable Hg/TOC anomalies.

Despite that, all sections except for Abadeh, display a short-lived Hg/TOC spike in the latest Permian mass extinction (LPME) horizon, labeled here as spike I (at Meishan, in the top of the bed # 24 (24E) and bed # 25). With the exceptions of Seres/Misci and Zal, the other six sections display a less pronounced Hg/TOC spike at the Permian–Triassic boundary (PTB), labeled here as spike II. Five of these sections exhibit a discrete (Zal, Abadeh, Ursula Creek and Meishan) to large (Rizvanuša) Hg/TOC spike at the Early Triassic mass extinction (ETME) horizon, labeled as spike III. In addition, with the exception of Idrijca, seven of these sections display a Hg/TOC spike between the LPME and the PTB (at Meishan is in bed # 26) and corresponds to a discrete positive $\delta^{13}C_{carb}$ excursion (in the $\delta^{13}C_{carb}$ negative trend). Similar anomaly has already been reported elsewhere from a shallow-marine section at Xiakou, China, and a deeper-marine section at Akkamori, Japan (Shen et al., 2019a).Only the Misci and Zal sections show a Hg/TOC spike at about 10 cm below the LPME (Figs. 4 and 7).

The normalization of Hg against TOC in these sections has consistently led to Hg/TOC anomalies at the LPME and PTB, suggesting that these are true Hg loading to the environment, although some of them probably represent exaggerated Hg/TOC ratios due to very low TOC values. The Hg/TOC spike between the LPME and the PTB in all but at Idrijca is, perhaps, also a primary feature. The spike III, less prominent than spikes I and II except in the Rizvanuša section, is absent from three among the eight studied sections, perhaps due to depositional hiatus, erosion or local secondary processes.

The Hg and Hg/TOC pathways in the Idrijca section increase steadily immediately above the PTB in a way that departs from the rest of the examined sections. A potential explanation is that Hg has been contaminated in at least part of the Idrijca rocks due to Permo-Carboniferous to Middle Triassic hydrothermal Hg mineralizing activity in the region (Lavric and Spangenberg, 2003; Foucher et al., 2009).

A NW–SE Hg/TOC transect disposed diagonally to the Pangaea supercontinent, passing through seven of the studied sections (from Ursula Creek in Canada to Hovea-3 in Australia, leaving the Meishan section aside as it lies in the opposite side of the Palaeo Tethys as shown in Fig. 1) is found in Fig. 12. In building this transect, the position of the LPME and ETME horizons have been kept as shown in their original figures (Figs. 4 through 7 and from 9 through 11) and the PTB has been used as the datum. From this attempt to attain a global picture of the Permian–Triassic transition, it becomes clear that Hg/TOC patterns throughout the studied sections are similar to each other and a strong variation of sedimentation rates becomes evident.

Apparently, clay was another Hg host besides organic carbon in these sections. Extensive continental weathering followed the LPME (Zhang et al., 2018) leading to generation of clays that were subsequently deposited along carbonates forming marls, marly limestones, shales or mudstones between the LPME layer and the P − T boundary (Algeo and Twitchett, 2010). Mercury peaks observed in this interval, in almost all of the studied PTB sections, perhaps denounce the presence of clays on which Hg has been partially adsorbed onto.

5.2. Mercury isotopes

It is known that Hg isotopes undergo large mass-dependent (MDF) and mass-independent (MIF) fractionations in nature and these signatures can potentially shed some light in tracing Hg sources (e.g., Blum et al., 2014) and pathways of Hg and Hg/TOC excursions (e.g.

Table 1
TOC (%). Hg(ng·g^{-1})and Hg/TOC compositions of representative samples from Permian–Triassic sections at Ursula Creek (Canada), Misci (Seres, Alps), Idrijca (Slovenia), Rizvanuša (Croatia), Zal and Abadeh (Iran), Meishan (China) and Hovea-3 well, onshore Perth Basin, Western Australia.

Sample	Height (m)	$\delta^{13}C_{carb}$(‰) vs. V-PDB	$\delta^{13}C_{org}$(‰) vs. V-PDB	TOC (%)	Hg (ng·g^{-1})	Hg/TOC
(a) Ursula Creek. Canada						
UC-1	0.5			0.08	31.68	396.0
UC-3	3.7			0.10	27.99	279.9
UC-6	8			0.07	14.27	203.9
UC-9	10			0.06	22.34	372.3
UC-12	12.9			0.05	26.56	531.2
UC-13	12.5			0.12	29.76	248.0
UC-14	14.2			0.15	54.27	361.8
UC-17	15.6			0.12	67.53	562.8
UC-18	15.9			0.32	24.48	76.5
UC-19	16		−29.70	0.31	55.65	179.5
UC-20	16.1			0.50	68.97	137.9
UC-22	16.4		−27.40	0.45	23.34	51.9
UC-25	17.3		−28.46	0.80	308.35	385.4
UC-28	18.25		−32.57	0.50	43.21	86.4
UC-31	19.9		−32.15	0.80	249.38	311.7
UC-33	22		−29.90	0.90	460.35	511.5
UC-34	24			0.54	167.51	310.2
UC-35	26			0.67	154.42	230.5
UC-36	29			0.76	138.78	182.6
UC-37	32			1.10	132.39	120.4
UC-38	36			1.30	123.17	94.7
UC-40	39			1.60	31.66	19.8
UC-41	42			0.89	42.02	47.2
UC-41.5	44			1.10	80.57	73.2
UC-42	46			0.80	65.93	82.4
UC-43	48			0.30	48.68	162.3
UC-44	50			0.32	30.23	94.5
(b) Misci (Seres, Southern Alps)						
Ser-1	0.15	2.42	−25.07	0.07		
Ser-2	1.15	2.89	−26.39	0.02		
Ser-3	3.65	2.48	−26.3	0.07		
Ser-4	4.35	3.17	−26.3	0.04	13.3	333
Ser-5	5.55	3.21	−24.93	0.04		
Ser-6	6.75	3.53	−24.67	0.05	10.5	210
Ser-7	7.55	3.57	−25.67	0.04		
Ser-8	7.95	3.86	−25.96	0.02	11.2	560
Ser-9	8.45	2.64	−28.31	0.08	9.5	119
Ser-10	8.95	3.13	−29.91	0.2	15	75
Ser-101 (event layer)	9.05	2.98	−24.9	0.12	29	242
Ser-11	9.22	2.73	−29.75	0.06	12.8	213
Ser-12	9.3	1.42	−28.47	0.02	24.8	1240
Ser-13	9.48	0.74	−29.07	0.02		
Ser-14	9.57	1.16	−27.3	0.02		
Ser-15	9.75	1.02	−27.68	0.02		
Ser-16	9.91	1.02	−26.23	0.01	11.4	1140
Ser-17	10	0.79	−28.07	0.12	7.8	65
Ser-18	10.29	1.01	−26.51	0		
Ser-19	10.38	1.03	−28.8	0.01		
Ser-20	10.565		−26.34	0.03		
Ser-21	10.813	1.19	−28.91	0.02	11.3	565
Ser-22	10.975	0.88	−28.66	0.02		
Ser-23	11.095	0.94	−28.57	0.02		
Ser-24	11.335	0.37	−30.05	0.02		
Ser-25	11.435	0.47	−29.27	0.01		
Ser-26	11.8	0.2	−29.6	0.01	10.9	1090
Ser-27	12.055	0.46	−30.03	0.02		
Ser-28	12.6	0.39	−27.67	0.01		
Ser-29	13.195	−0.09	−29.58	0.01		
Ser-30	13.57	0.09	−29.33	0.01		
Ser-31	13.8	−0.25	−28.93	0.02	8.7	435
Ser-32	14.32	−0.3	−28.89	0.02		
Ser-33	14.51	−0.54	−29.12	0.02	3.3	165
Ser-34	14.88	−0.32	−29.48	0.01		
Ser-35	19.15	−2.33	−29.76	0.04		
Ser-36	19.65	−2.22	−30.85	0.05		
Ser-37	21.69	−3.74	−32.56	0.11		
Ser-38	21.99	−1.87	−30.79	0.04		
Ser-39	23.39	−1.61	−30.84	0.03		
(c) Idrijca section (Idrjca Valley). Slovenia						
J-4b (VS-12)	−1.2	3	−28.4	0.28	930.18	3322
J-3a (VS-11)	−0.9	2.4	−27.9	0.24	907.26	3780

(*continued on next page*)

Table 1 (*continued*)

Sample	Height (m)	$\delta^{13}C_{carb}$(‰) vs. V-PDB	$\delta^{13}C_{org}$(‰) vs. V-PDB	TOC (%)	Hg (ng·g^{-1})	Hg/TOC
J-3b (VS-10)	−0.7	2.2	−27.6	0.2	831.89	4159
J-2b (VS-9)	−0.6	2.2	−26.7	0.17	937.44	5514
Job/a (VS-8a)	−0.2	1.2	−27.4	0.13	910.14	7001
Job/b(VS-8b)	−0.15	1	−26.7	0.11	490.79	4462
Jo (VS-8)	−0.1	1.2	−26	0.14	458.4	3274
IA-1/2 (VS-7)	0	1.1	−26.1	0.17	598.9	3523
IA-3 (VS-6)	0.1	1.3	−25.9	0.16	479.45	2997
IA-4/5(VS-5)	0.3	0.8	−25.4	0.1	544.16	5442
IA-7 (VS-4)	0.7	0.7	−25.7	0.11	784.46	7131
IA-9 (VS-3)	1.2	0.5	−27.1	0.1	1092.39	10,924
(d) Rizvanuša, Velebit Mountain, Croatia						
PTR-35	−2.70	1.33	−26.3	0.006	30.89	5370
PTR-44	−0.90	1.40	−28.6	0.014	10.18	713
PTR-45	−0.70	1.70	−28.6	0.008	180.09	21,893
PTR-46	−0.50	1.89	−28.6	0.028	7.21	254
PTR-47	−0.30	1.02	−28.6	0.008	181.58	23,670
PTR-48	−0.10	1.48	−28.4	0.013	33.64	2509
PTR-49	0.10	−0.03	−29.2	0.030	284.80	9606
PTR-50	0.30	0.71	−28.8	0.010	42.90	4469
PTR-50/51	0.40	0.45	−29.1	0.011	70.51	6235
PTR-51	0.50	0.01	−29.6	0.024	299.29	12,722
PTR-52	0.70	0.04	−29.3	0.022	189.52	8682
PTR-53	0.90	0.03	−29.1	0.020	42.47	2131
PTR-59	2.10	0.48	−32	0.034	21.79	644
(e) Zal, Iran						
Zal-19	0	3	–	0.03	19.6	653
Zal-18	0.70	2.8	−26.67	0.01	19.9	1990
Zal-17	2.30	2.6	−26.67	0.02	21.6	1080
Zal-16	2.40	2.4	−26.50	0.03	38.1	1270
Zal-15	2.43	2.4	−27.71	0.01	19.9	1990
Zal-14	2.46	2.2	−27.73	0.02	58.6	2930
Zal-13	2.48	2.1	−25.59	0.04	62.7	1567
Zal-11	2.61	1.8	−26.10	0.01	27	2700
Zal-10	2.64	1.5	−27.27	0.02	51.6	2580
Zal 9/10 (event layer)	2.66	1.3	−26.45	0.03	88.96	2953
Zal-9	2.67	1.3	−27.75	0.02	60.9	3045
Zal-8	2.77	1.1	−27.08	0.02	45.6	2280
Zal-7	3.07	0.8	−26.29	0.01	32.4	3240
Zal-6	3.19	1.2	−28.34	0.02	49.5	2475
Zal-5	3.31	0.6	−27.09	0.02	86	4330
Zal-4	3.86	0.4	−29.10	0.01	10.95	1095
Zal-3	4.11	−0.5	−31.11	0.01	17.84	1784
Zal-2	4.91	0	−29.22	0.02	12.48	624
Zal-1	5.28	−0.1	−30.77	0.03	23.12	770
(f) Abadeh section, Iran						
Aba-47	47.80	3.26	−27.82	0.005	2.0	400
Aba-56	50.38	2.02	−25.80	0.007	2.0	285
Aba-61	50.93	0.62	−24.60	0.008	2.4	300
Aba-66	51.38	0.99	–	0.008	9.6	1200
Aba-66-2					9.52	
Aba-68a	51.81	1.12	−27.22	0.012	2.1	175
Aba-68d	52.31	−0.12	−28.57	0.012	4.6	383
Aba-70	52.70	−0.08	−26.71	0.015	3.0	200
Aba-72	53.40	−0.32	−25.68	0.009	10.8	1200
Aba-73	53.60	−0.30	−25.68	0.009	2.6	289
Aba-76	55.00	–	−25.94	0.005	19.9	3980
(g) Meishan section, China						
Meishan-1	−273	4.7	−26.95	0.10	6.1	61
Meishan-2	−238	4.0				
Meishan-3	−198	3.6	−26.66	0.15	5.0	33.33
Meishan-4	−179	4.0				
Meishan-5	−168	4.2				
Meishan-6	−113	4.1	−28.84	0.53	14.7	27.73
Meishan-7	−106.5	3.7				
Meishan-8	−88	2.7	−30.05	1.87	26.6	12.24
Meishan-9	−73	2.5				
Meishan-10	−68	2.6				
Meishan-11	−68	2.6	−27.26	0.06	1.5	25
Meishan-12	−57	2.3				
Meishan-13	−56.5	2.5				
Meishan-14	−54.5	2.6				
Meishan-15	−22.5	2.1	−29.59	0.20	8.8	44
Meishan-16	−15	2.0				

(*continued on next page*)

Table 1 (*continued*)

Sample	Height (m)	$\delta^{13}C_{carb}$(‰) vs. V-PDB	$\delta^{13}C_{org}$(‰) vs. V-PDB	TOC (%)	Hg (ng·g^{-1})	Hg/TOC
Meishan-17	−15	2.1				
Meishan-18	−9	1.9				
Meishan-19	−7.5	2.2				
Meishan-20	−7.5	2.2	−27.82	0.20	15.1	75.5
Meishan-21	−5.0	2.0				
Meishan-22	−3.5	1.8				
Meishan-23	−3.5	1.9	−28.03	0.09	3.6	40
Meishan-50 (24E top)	−0.1			0.11	346.4	3149.09
Meishan-51A	+0.8		−28.52	0.49	32.9	67.14
Meishan-51B	+1.9		−26.26	0.05	21.0	420
Meishan-24	+6.5	−1.0	−30.49	0.57	122.3	214.56
Meishan-25	+6.5	−1.1				
Meishan-26	+10.5	0.0	−26.23	0.07	46.9	670
Meishan-27	+10.5	0.0				
Meishan-28	+12.5	0.2				
Meishan-29	+15.0	0.1	−26.64	0.04	13.0	325
Meishan-30	+15.0	0.0				
Meishan-31	+18.0	0.3				
Meishan-32	+18.0	0.2				
Meishan-33	+20.5	0.7	−26.22	0.05	9.3	186
Meishan-34	+22.5	0.8				
Meishan-35	+22.5	0.5				
Meishan-36	+25.5	0.1	−25.68	0.05	9.3	186
Meishan-37	32.5	1.2				
Meishan-38	+36.5	1.2	−26.50	0.05	6.5	130
Meishan-39	+45.0	0.9				
Meishan-40	+56.5	0.88	−27.64	0.12	32.3	269.16
Meishan-41	+68.7		−24.97	0.05	26.8	536

(h) Hovea-3 well, onshore Perth Basin, Western Australia

Black shale samples

Sample name	Core depth (m)	$\delta^{13}C_{org}$(‰) vs. V-PDB	TOC	Hg (ng·g^{-1})	Hg/TOC
Hov-1	1969.1	−33.8	2.3	39.25	17.1
Hov-2	1973.29	−35.1	1.5	55.11	36.7
Hov-3	1977.19	−35.9	1.2	111.67	93.1
Hov-4	1979.13	−35.7	2.5	207.33	82.9
Hov-5	1980	−35.7	1.9	77.98	41.0
Hov-6	1980.94	−36.3	1.5	158.74	105.8
Hov-7	1980.95	−36.2	1.6	108.1	67.6
Hov-8	1980.96	−36.3	1.7	273.36	160.8
Hov-9	1980.98	−35.9	1.7	123.77	72.8
Hov-10	1980.99	−35.6	1.8	96.73	53.7
Hov-11	1981.1	−34.1	3.9	77.21	19.8
Hov-12	1981.23	−34.9	2.3	97.43	42.4
Hov-13	1982.1	−34.8	2.2	78.58	35.7
Hov-14	1982.4	−31.9	0.8	92.01	115.0
Hov-15	1982.73	−31.3	1.2	77.3	64.4
Hov-16	1982.94	−31.1	1.5	75.86	50.6
Hov-17	1983.48	−30.4	0.8	437.05	546.3
Hov-18	1984.7	−27.3	0.9	62.28	69.2
Hov-19	1984.95	−27.6		116.07	

Thibodeau et al., 2016; Grasby et al., 2017; Gong et al., 2017; Wang et al., 2018). Mass-dependent fractionation can be triggered and modified by physical, chemical or biological reactions, this should be considered when tracing the source for Hg in environment. However, as Hg-MIF signatures are unlikely altered by post-depositional processes according to Smith et al. (2008), MIF would be more useful for source identification Shen et al., 2019a,b).

Hg isotopes have been analyzed in a total of twenty-five samples from the studied Permian–Triassic sections (Table 2). Most of the selected samples are from the mass extinction interval indicated in these sections, with high Hg/TOC values. Mass dependent fractionation (MDF) reported as δ^{202}Hg values are all negative in this study, sixteen of them within the −2.00 to −0.85% range, eight from −2.20 to −3.00% and one sample yielded a much lower value of −3.79% (Table 2).

In a δ^{202}Hg vs Δ^{201}Hg (MIF) diagram, almost 70% of the analyzed samples plot within the volcanic-emission box (Fig. 13a). Four horizontal trends are evident in this figure. Three samples from the Abadeh section together with the sample ZAL 9/10 (event layer at Zal section) define the **trend I** in this diagram with positive Δ^{201}Hg (MIF) values. Samples from the three sections in Europe (Rizvanuša, Seres/Misci and Idrijca) together with one from Hovea-3 define the **trend II**, exhibiting Δ^{201}Hg values around zero. Five samples from Meishan (beds # 24, 26, 40, 50, 51A) show very consistent values that cluster within the **trend III** in the volcanic-emission box together with two samples from Ursula Creek and one from Hovea-3, showing slightly negative Δ^{201}Hg values. Likely Hg in the samples from Meishan originated from one same source, with negligible or none Δ^{201}Hg (MIF) fractionation during atmospheric transport and the same happened with Rizvanuša samples in trend II. Besides, the total range of measured Δ^{199}Hg values (−0.10–0.00) within the Permian–Triassic mass extinction interval in Rizvanuša, Meishan, Seres/Misci, Idrijca and Zal sections fall within

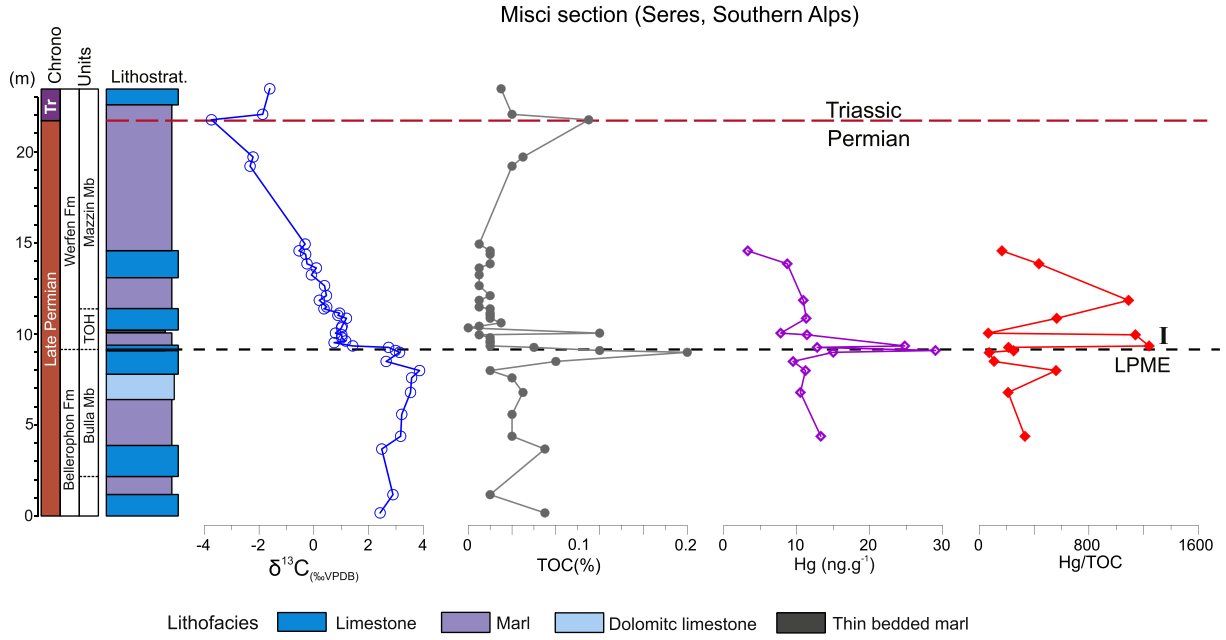

Fig. 4. Stratigraphy, lithology, carbon isotope ratios (Kraus et al., 2013), Hg, TOC concentrations and Hg/TOC (this study) of the Seres/Misci section, Southern Alps. LPME stands for latest Permian mass extinction and TOC, for total organic carbon in this and subsequent figures.

experimental error of zero, a possible evidence for a significant influx of volcanic Hg in this time interval. Small positive Δ^{201}Hg favors long-term atmospheric transport and support Hg loading to the environment by the STLIP magmatism. There is a possibility that the negative values displayed by δ^{202}Hg MDF (−1.07 to −1.79) and Δ^{199}Hg (0.00 to −008) in samples from Meishan in **trend III** can be explained by presence of a significant proportion of Hg from terrestrial sources as suggested elsewhere by Grasby et al. (2017), Wang et al. (2018) and Shen et al. (2019a,b). The **trend IV** is composed of three samples from the Zal section which exhibit the lowest negative Δ^{201}Hg (MIF) values, in contrast with the Zal 9/10 event layer which exhibits the highest positive Δ^{201}Hg (MIF) value among the studied samples. In summary, the two sections from Iran exhibit the highest (**trend I**) and the lowest (**trend IV**) Δ^{201}Hg (MIF) values in this study.

A total of seven samples (Zal, Ursula Creek, Idrijca and Abadeh) plot in the sediment, soil and peat box in the δ^{202}Hg vs Δ^{201}Hg diagram (Fig. 13a). In these samples, Hg (MDF) isotopes seem to have suffered further fractionation that has pushed δ^{202}Hg values towards more negative values due to terrestrial Hg influx. One cannot discard, however, that this feature could be also a consequence of a coal-source triggered by the contemporary intrusive stage 2 of the STLIP sill complex of Burgess et al. (2017).

In an attempt to compare Hg isotope behavior during mass extinction events in the Permian–Triassic and Cretaceous–Paleogene (K/Pg) boundaries, a δ^{202}Hg vs Δ^{201}Hg diagram for four Cretaceous–Paleogene boundary sections (Fig. 13b) is shown (modified from Sial et al., 2019). For this boundary, two trends roughly parallel can be depicted from this figure: (a) **spike II trend** generated by Hg/TOC analyses from a thin K/Pg boundary clay layer from K/Pg sections at Højerup (Stevns Klint, Denmark), Bottaccione (Gubbio, Italy), Sohryngkew (Meghalaya, India) and Bidart (Basque Basin, France); and (b) **spike III trend** formed by samples from the P1a planktic foraminiferal subzone from the Bidart France and the Poty Quarry (Brazil) sections. Samples in the **spike II trend** display Δ^{201}Hg around zero and Hg has been regarded as loaded

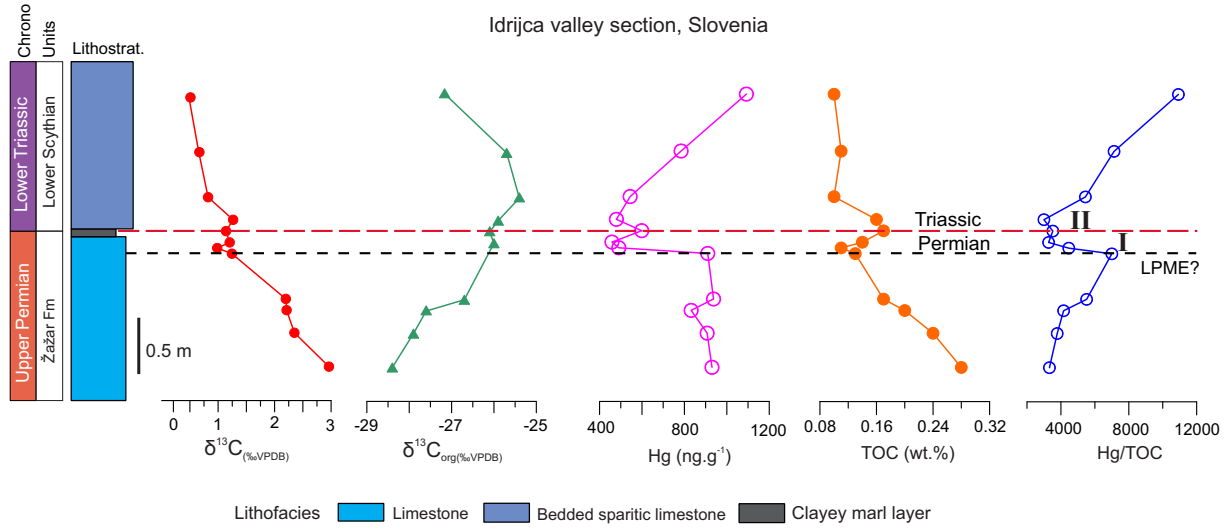

Fig. 5. $\delta^{13}C_{carb}$, $\delta^{13}C_{org}$ (Schwab and Spangenberg, 2004), Hg, TOC and Hg/TOC (this study) variation patterns for the Idrijca Valley section (Slovenia).

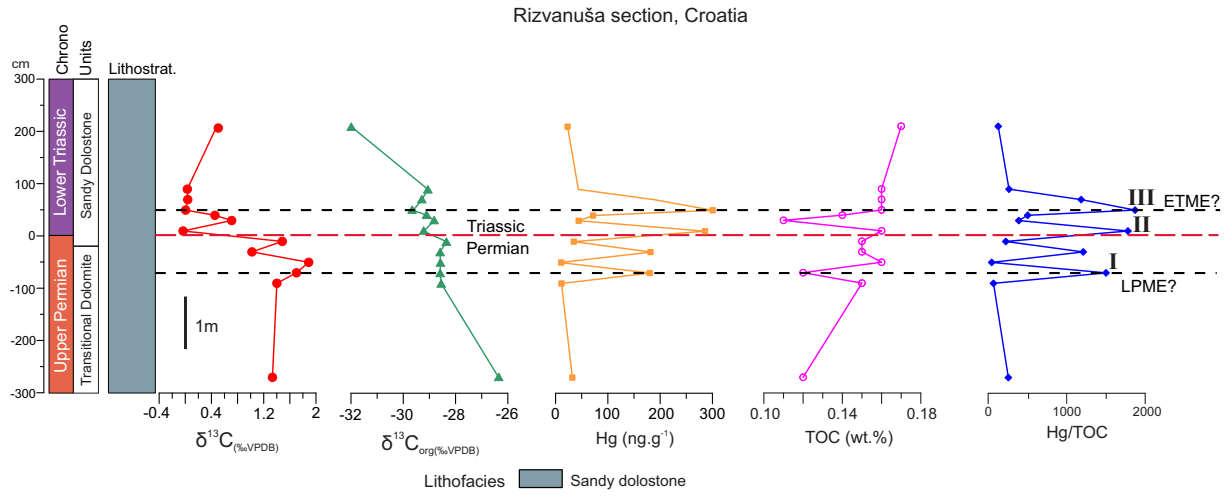

Fig. 6. $\delta^{13}C_{carb}$ variation pattern (Fio et al., 2010) and Hg, TOC concentrations and Hg/TOC (this study) of the Rizvanuša stratigraphic section, Velebit Mountains, Croatia.
LPME and ETME stand, respectively, for latest Permian and Early Triassic mass extinctions.

by the Deccan volcanism or it is extraterrestrial in nature from the asteroid impact at Chicxulub (Sial et al., 2019). Just one sample in this trend (from Højerup) plotted inside the sediment, soil and peat box, suggesting that samples in this trend have not undergone significative Hg-MIF fractionation during atmospheric transport, except for one sample that may have faced Hg-MDF change by some terrestrial influx. As it is unlikely that post-depositional processes change Hg-MIF signatures, the **spike II trend** is probably a primary one, generated by Hg from the Deccan volcanism.

Two main differences between the behavior of Hg isotopes in the Permian–Triassic and Cretaceous–Paleogene transitions can be drawn from this study: (a) some K/Pg boundary clay layer samples plot within the chondrite/volcanic emission box, something which not observed among PTB samples; (b) Hg in K/Pg clay layer samples defines a well-delineated **spike II trend**, without much Hg-MIF fractionation during transport from the Deccan volcanic site or further change in the local of deposition. Samples in the PTB **trend II** are likely Hg from the STLIP volcanism but with small degree of terrigenous Hg influx in the site of deposition.

In summary, from the δ^{202}Hg vs Δ^{201}Hg crossplot it can be concluded that volcanic Hg isotopes in the K/Pg boundary have received little terrigenous-Hg influx influence. In contrast, at the PTB, volcanic Hg has received variable influence from terrigenous-source influx, more intense in samples in **trends III and IV** (Meishan, Ursula Creek, Zal and Hovea-3 sections, which are far distant from the STLIP), but less intense in **trend II** samples (Seres/Misci, Rizvanuša and Idrijca sections, in Europe, which are relatively closer to the STLIP).

In a recent study on two continental Permian–Triassic sections of the South China Craton, Shen et al. (2019b) have shown that pre- and post-event beds are characterized by low Hg concentrations and more positive values of MIF odd Hg isotopes, whereas the mass extinction interval is characterized by higher Hg concentrations and lower MIF odd Hg isotope values (usually negative values). From the crossplot of Δ^{199}Hg versus Hg concentrations, can be concluded that samples tend

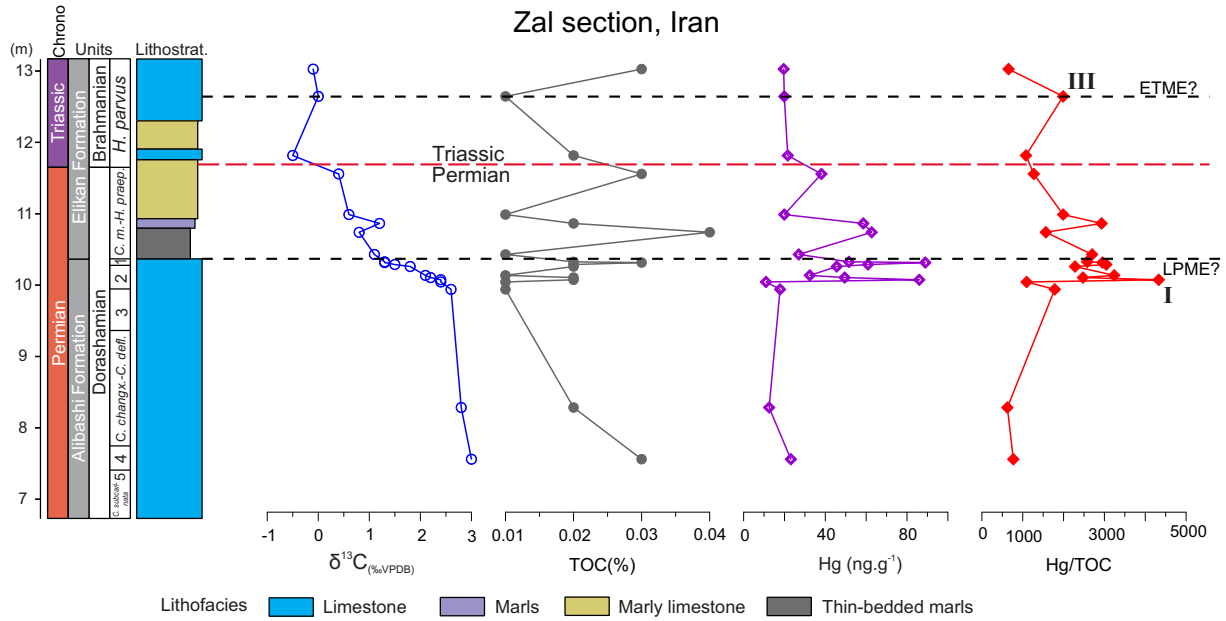

Fig. 7. Lithologic succession, biostratigraphy and $\delta^{13}C_{carb}$ chemostratigraphy (Korte et al., 2004a,b,c) and Hg, TOC and Hg/TOC for a Zal stratigraphic section, Iran (this study).

Fig. 8. Photograph of the Meishan section in this study, China (Permian–Triassic boundary GSSP; photo taken by Christoph Korte).

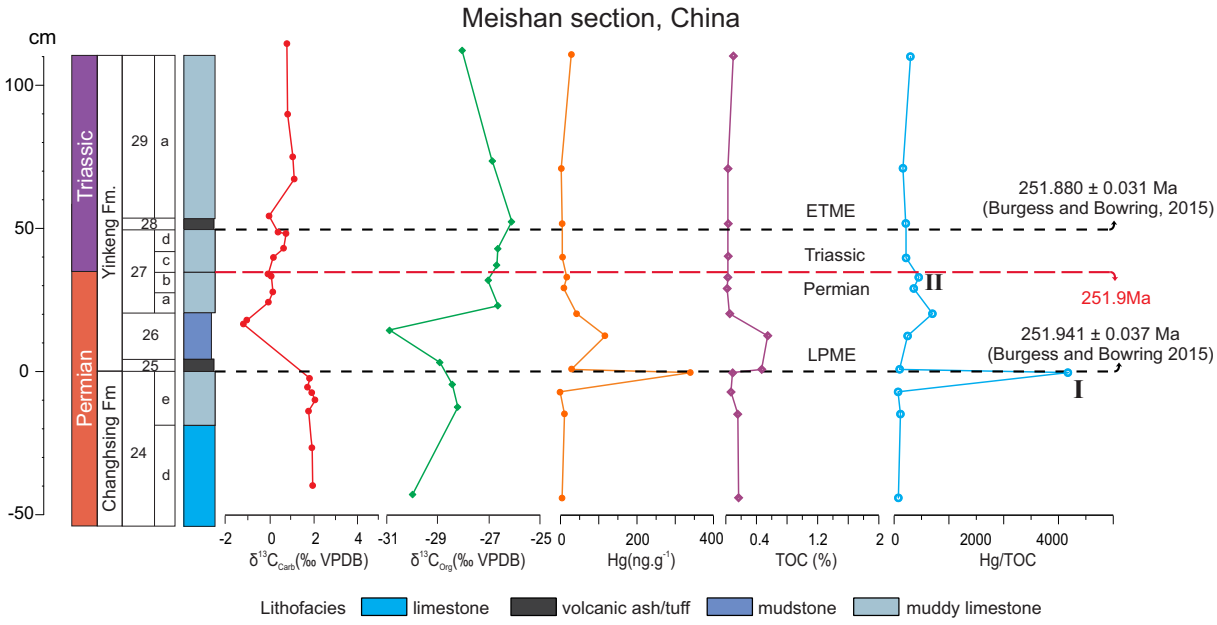

Fig. 9. Lithological succession according to Chen et al. (2015); $\delta^{13}C_{carb}$ variation pattern is from Jin et al. (2000). $\delta^{13}C_{org}$, Hg, TOC and Hg/TOC chemostratigraphic pathways are from the study.

to fall along a mixing trend defined by a background endmember with low Hg and high MIF and a volcanic endmember with high Hg and low MIF.

A crossplot between Δ^{199}Hg ‰ (MIF) and Hg ($ng \cdot g^{-1}$) for the eight sections investigated in this study display two curved trends (Fig. 14a), likely determined by two-component mixing between marine sediment and volcanic-source Hg. The **trend I** (three samples from Abadeh) exhibit positive Δ^{199}Hg values while two samples from Meishan and one from Ursula Creek display negative values. In **trend II**, three samples from Zal and one from Misci display positive values, while three samples from Meishan and two from Hovea-3 and two from Ursula Creek and three from Rizvanuša sections display Δ^{199}Hg (MIF) around zero or with negative values. The sample Zal 9/10 (event layer) departs from this trend more than any other sample in the trend. Perhaps, this is a consequence of input from rapid erosion of Hg from soils as invoked to explain a similar situation in China (Shen et al., 2019b).

Three samples from the Idrijca section (**trend III**) show positive Δ^{199}Hg (MIF) values and the highest Hg contents among the studied sections. These samples may have been strongly affected by hydrothermal Hg contamination from the Idrijca mining region (Permo-

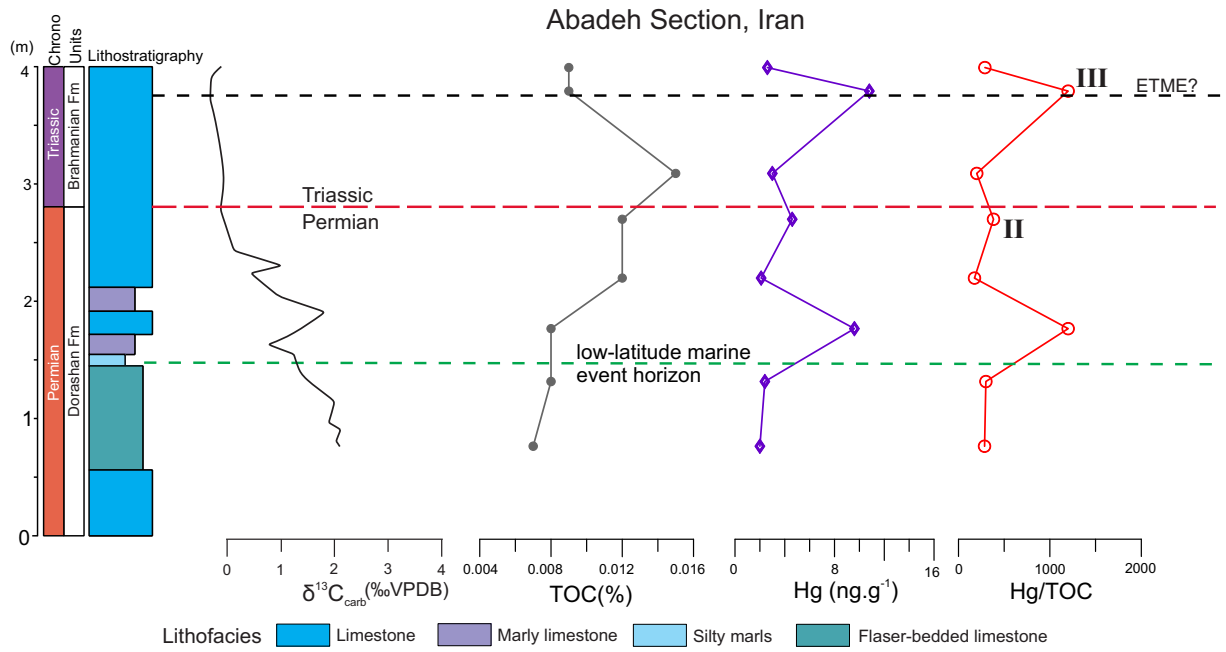

Fig. 10. Lithology and conodont zonation of the Permian–Triassic transition section at Abadeh, Iran, according to Korte et al. (2004a,b,c). Hg, TOC and Hg/TOC variation patterns are from this study.

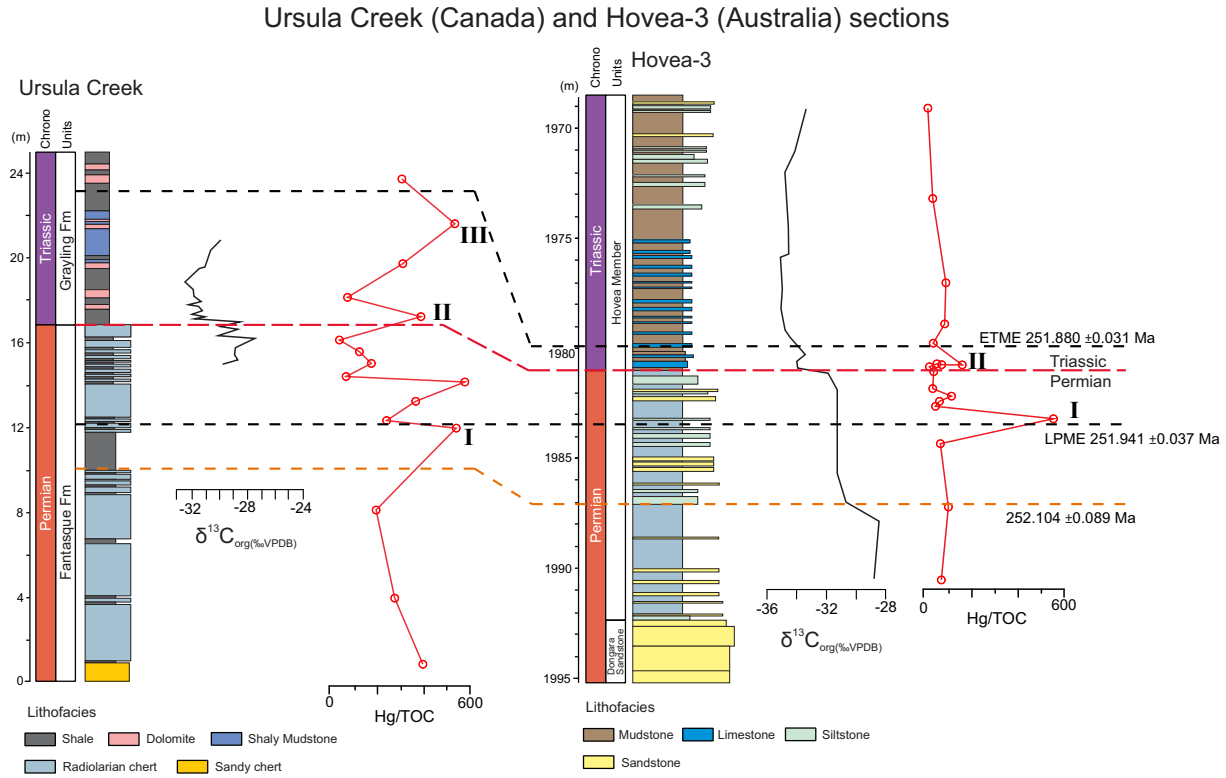

Fig. 11. Permian–Triassic boundary sections at Ursula Creek and Hovea-3. For the former, lithological and $\delta^{13}C_{org}$ variation patterns are, respectively, from Wignall and Newton (2003) and Wang et al. (1994) while for the latter, lithological column and $\delta^{13}C$ are from Thomas et al. (2004). Hg/TOC variation patterns for both sections are from the present study.

Carboniferous to Middle Triassic hydrothermal Hg mineralizing activity in the region) (Lavric and Spangenberg, 2003; Foucher et al., 2009). This has led to much higher Hg concentrations than seen in any other section (e.g., Ursula Creek and Idrijca exhibit similar TOC values but Hg is much higher at Idrijca). Two samples from the Ursula Creek section plot in the vicinity of the **trend III**, a behavior for which we found no clear explanation.

A Δ^{199}Hg ‰ (MIF) versus Hg ($ng{\cdot}g^{-1}$) cross plot for the K/Pg transition using the data available in Sial et al. (2019) is shown in Fig. 14b. The number of analyses in this case is more limited than for the PTB. Except for two samples (**spike III trend**) from the Poty Quarry (Brazil), collected about one meter above the K/Pg boundary, and one

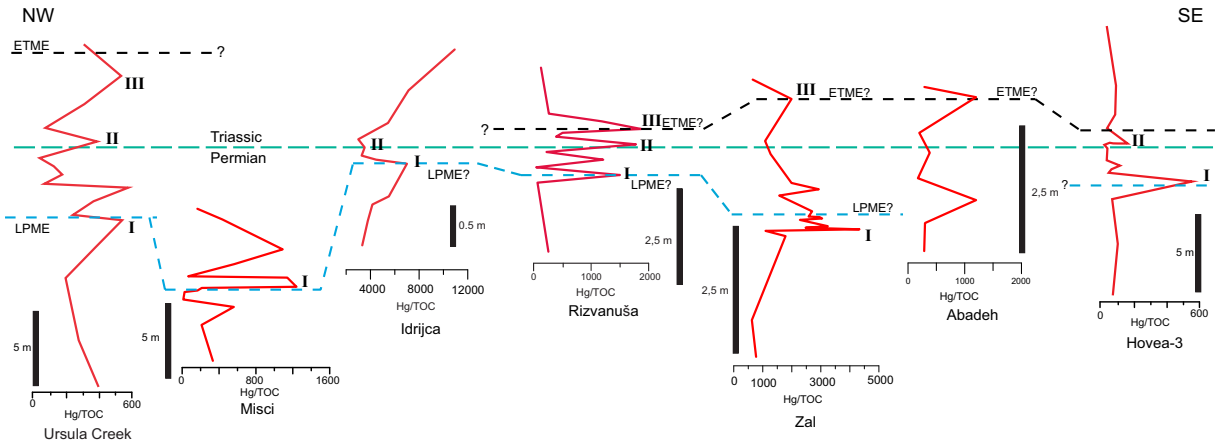

Fig. 12. NW–SE Hg/TOC transect diagonal to the Pangea supercontinent about 252 Ma ago, passing through seven of the studied sections (from Ursula Creek in Canada through Hovea-3 in Australia). In building this transect, the position of the LPME and ETME horizons have been kept as shown in their original figures (Figs. 4 through 7 and 9 through 11) and the PTB datum was used.

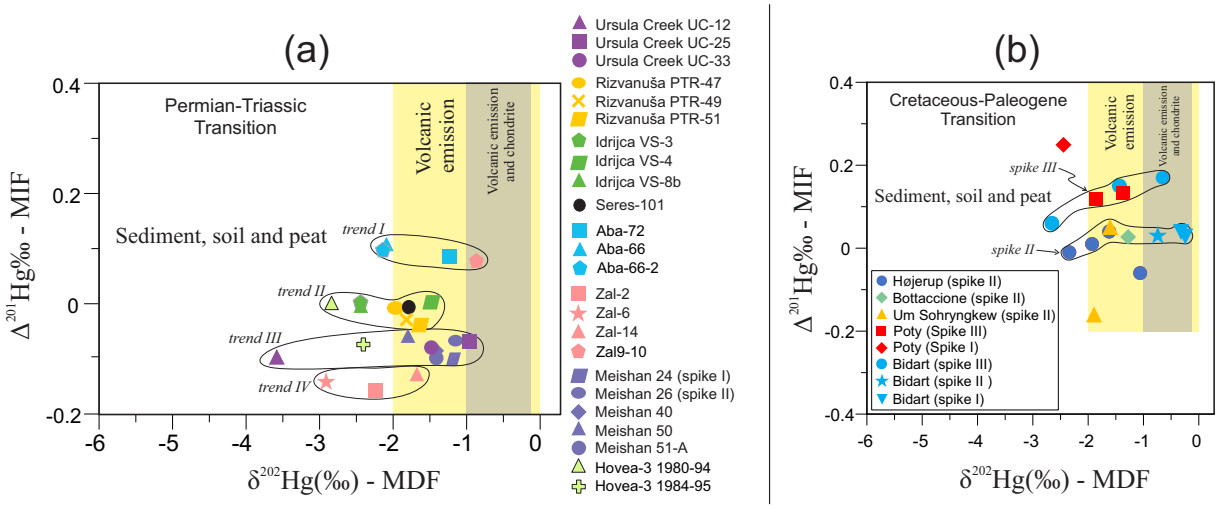

Fig. 13. (a) In a δ^{202}Hg‰ (MDF)–Δ^{201}Hg (MIF) diagram, most of the analyzed samples plot within the volcanogenic Hg emission box and display three trends: trend I is formed by Rizvanuša, Seres/Misci and Idrijca samples; trend II by Meishan and Ursula Creek samples and trend III, by Zal samples. Four samples plotted within the sediment, soil and peat box. (b) A δ^{202}Hg ‰ (MDF)–Δ^{201}Hg‰ plot for the Cretaceous–Paleogene transition (modified from Sial et al., 2019) is added for comparison. While Δ^{201}Hg‰ (MIF) values tend to be negative in the PTB transition, they tend to be slightly positive to zero in the K/Pg transition. Two trends are displayed by the K/Pg samples: Hg/TOC spike II trend (K/Pg layer) and Hg/TOC spike III (slightly above the K/Pg). Ranges for (i) volcanogenic, (ii) chondritic Hg and (iii) sediment, soil and peat are based on Bergquist and Blum (2009) and are shown as vertical bars.

from Um Sohryngkew (India) all samples from the K/Pg layer (**spike II trend**) consistently display Δ^{199}Hg ‰ (MIF) values around zero. Fig. 14b confirms what has been stated above about Fig. 13b, that odd Hg-MIF isotopes in **spike II** have undergone negligible to none fractionation from the Deccan volcanic center to the local of deposition. Two-component mixing between volcanic and terrigenous Hg influx at the **spike II** seems to have been more limited than in the PTB layers.

6. Conclusions

In most of the marine PTB sections in this study, TOC exhibits rather low values (usually < 0.20 wt%). Even so, Hg/TOC yielded consistently three to four spikes in almost all sections whose assessment leads to the following conclusions: (a) pronounced increase in Hg/TOC values at the LPME event reveals a coincident, robust synchronism between LPME and STLIP magmatism; (b) a NW-SE diagonal transect across the Pangaea supercontinent (252 Ma ago), reveals that Hg/TOC patterns of the studied sections are similar to each other and that there was a strong variation in sedimentation rates across the extinction interval. This demonstrates that Hg/TOC maybe has some potential to be used in stratigraphic correlation; (c) The PTB and K/Pg were associated to LIP volcanism but the variation trends of Δ^{199}Hg with Hg concentrations for these two major chronological boundaries are very distinct. The Δ^{199}Hg values for the Hg peaks near the K/Pg are close to zero, but the Δ^{199}Hg for Hg peaks near PTB are the record of both terrigenous and volcanic sources, lower terrigenous Hg influx in settings closer to the STLIP, but higher in settings far distant to that. The possibility that these differences resulted from the depositional environment for each setting (e.g., various water-depth), not the distance from STLIP, cannot be totally discarded; (d) likely, the Deccan LIP volcanism has not affected the increase of land weathering as much as the STLIP. Alternatively, the STLIP magma went through organic matter-enriched beds (e.g., coal and black shale) and the Hg isotope data could represent different degree of mixture of volcanic Hg release (Δ^{199}Hg near 0) and Hg from organic matter-enriched sediments (negative Δ^{199}Hg). In this case, the Hg peaks in sediments could be negative. In the K/Pg, the near zero Δ^{199}Hg of Hg enrichment perhaps came only from the volcanic Hg release; (e) the negative C-isotope excursions and Hg/TOC enrichments are nearly coeval and this supports the hypothesis of synchronism between the Permian–Triassic transition biotic crises and the start of the

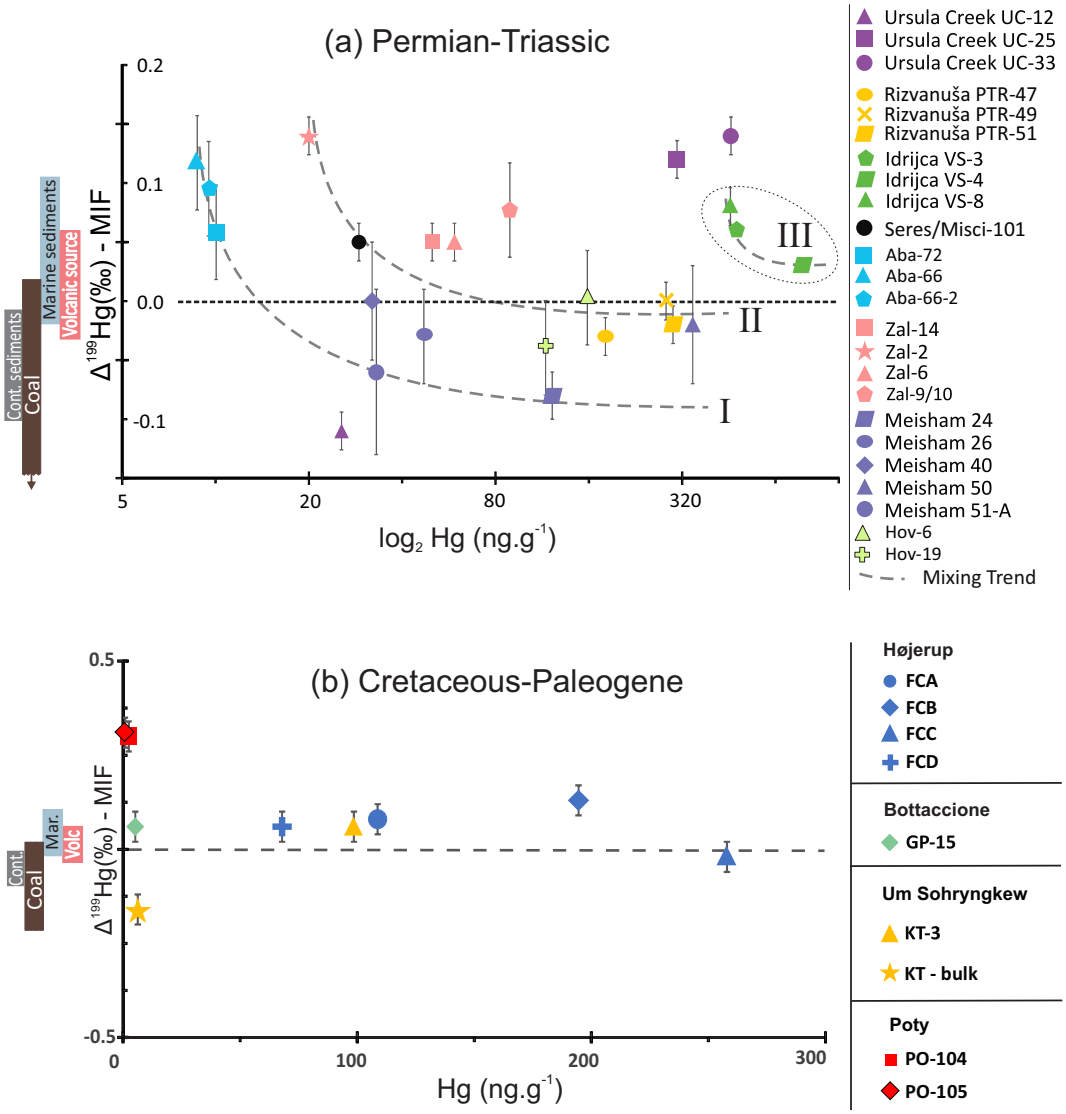

Fig. 14. (a) Crossplot between Δ^{199}Hg‰ (MIF) and $\log_2$Hg (ng·g^{-1}) for sections in this study. The four vertical bars to the left of the diagram are from Shen et al. (2019c). The four curved trends probably resulted from two-component mixing between normal marine sediment and volcanic-source Hg. Trends I (Meishan section) and II (Rizvanuša and Seres/Misci) are similar and close to each other. The trend III (Zal section) may have received an input of erosional concentration of Hg, and trend IV (Idrijca section) may have been strongly affected by a terrestrial Hg contamination from the Idrijca mining region; (b) A Δ^{199}Hg ‰ (MIF) versus Hg (ng·g^{-1}) cross plot for the K/Pg transition using the Hg data available in Sial et al. (2019) is shown in panel b. The four vertical colored bars to the left of the diagram in panel a are based on Shen et al. (2019c). Same in panel b where Volc = volcanic source, Mar. = marine sediments, Cont. = continental sediments. (For interpretation of the references to color in this figure legend, the reader is referred to the web version of this article.)

stage 2 of the Siberian Traps (late sill-intrusion style of magmatism, forming a sub-volcanic network of intrusions).

Declaration of competing interest

The authors declare that they have no known competing financial interests or personal relationships that could have appeared to influence the work reported in this paper.

Acknowledgments

Grants to ANS (CNPq 471036/2012-9, 407171/2018-5; FACEPE APQ-1059-9.05/12, 1073-1.07/15), to LDL (CNPq INCT-TMCOcean 573.601/2008-9, CNPq 576.601/2009-1), to VPF (CNPq 471034/2012-6; FACEPE APQ1738-1.07/12) and NSFC grants to JBC (41625012, U1612442, 41830647, 41561134017) provided financial support to chemical and/or isotope analyses. CK thanks the Freie Universität Berlin for sampling in South Tyrol and the Danish Natural Science Research Council for providing financial support for sampling in China and to QuanFeng Zheng for leading him in the field in Meishan (grant number 11-103378). JES acknowledges Tadej Dolenec for providing samples from the Idrijca Valley section, the FNS-SCOPES IB7320-110885 and the University of Lausanne for financial support for sampling of Croatian sections and all geochemical analyses. JCST wants to express his gratitude to Robert Newton and Paul Wignall by the cession of samples from Ursula Creek section and to Klity Grice for providing samples from the Hovea-3. We are grateful to Prof. Jun Shen (China University of Geosciences, Wuhan) and to an anonymous reviewer whose comments and suggestions on an earlier version of the manuscript greatly contributed to improve it. This is the NEG–LABISE scientific contribution n. 290.

Table 2
Hg isotopes (‰ relative to NIST SRM 3133) in samples from PTB sections at Meishan (GSSP section, China), Rizvanuša (Croatia), Misci (Seres, Southern Alps), Ursula Creek (Canada); Idrijca (Slovenia) and Zal (Iran). K/Pg sections with Hg enrichments: Um Sohryngkew, Poty; Højerup, Bottaccione (all from Sial et al., 2019). Analyses from Bidart (K/Pg) were added for comparison.

Samples	δ^{199}Hg	δ^{200}Hg	δ^{201}Hg	δ^{202}Hg	Δ^{199}Hg	Δ^{200}Hg	Δ^{201}Hg
Mass dependent fractionation (MDF)					Mass independent fractionation (MIF)		
Permian–Triassic Transition							
(a) Meishan, China (PTB, GSSP section)							
Layer-24	−0.35	−0.56	−0.93	−1.10	−0.08	0.00	−0.10
Layer-26	−0.29	−0.50	−0.90	−1.07	−0.03	0.04	−0.07
Layer-40	−0.34	−0.65	−1.12	−1.39	0.00	0.04	−0.09
Layer-50	−0.47	−0.85	−1.40	−1.79	−0.02	0.05	−0.06
Layer-51-A	−0.41	−0.67	−1.13	−1.38	−0.06	0.02	−0.10
(b) Rizvanuša (Velebit Mountain), Croatia							
PTR-47	−0.49	−0.93	−1.4	−1.82	−0.03	−0.02	−0.03
PTR-49	−0.50	−0.97	−1.5	−1.98	0.00	0.02	−0.01
PTR-51	−0.43	−0.80	−1.26	−1.62	−0.02	0.01	−0.04
PTR-52 (n = 3)	−0.72	−1.46	−2.22	−2.96	0.03	0.03	0.01
(c) Ursula Creek, Canada							
UC-12	−1.07	0.36	−2.95	−3.79	−0.11	2.23	−0.1
UC-25	−0.10	−0.41	−0.57	−0.85	0.12	0.02	0.07
UC-33	−0.22	−0.72	−1.0	−1.44	0.14	0.00	0.08
(d) Idrijca, Slovenia							
VS-3 (n = 3)	−0.58	−1.26	−1.89	−2.53	0.06	0.01	0.01
VS-4 (n = 3)	−0.33	−0.70	−1.08	−1.43	0.03	0.02	0.00
VS-8b	−0.56	−1.26	−1.87	−2.52	0.08	0.00	0.03
(e) Zal, Iran							
Zal-2	−0.44	−1.12	−1.57	−2.29	0.14	0.03	0.16
Zal-6	−0.71	−1.50	−2.14	−3.04	0.05	0.03	0.14
Zal-9/10 (event layer)	0.08	−0.38	−0.57	−0.86	0.08	0.06	0.08
Zal-14	−0.37	−0.82	−1.11	−1.65	0.05	0.01	0.13
(f) Abadeh, Iran							
ABA-72	−0.25	−0.58	−0.84	−1.23	0.06	0.04	0.09
ABA-66	−0.41	−1.00	−1.46	−2.08	0.12	0.04	0.11
ABA-66-2	−0.44	−0.99	−1.51	−2.14	0.10	0.08	0.10
(g) Seres/Misci, Southern Alps)							
Misci (Seres-101)	0.10	−0.81	−0.97	−1.76	0.05	0.08	−0.09
(h) Hovea-3							
1980–94 (Hov-6)	−0.71	−0.38	−2.13	−2.84	0.00	0.03	0.00
1984–95 (Hov-19)	−0.65	−1.19	−1.88	−2.40	−0.04	0.02	−0.07
Cretaceous–Paleogene Transition							
(f) K/Pg boundary layer at Højerup (Fiskeler Member), Denmark							
FCA	−0.51	−1.06	−1.76	−2.34	0.08	0.11	−0.01
FCB	−0.28	−0.74	−1.18	−1.62	0.13	0.07	0.04
FCC	−0.29	−0.55	−0.86	−1.06	−0.02	−0.02	−0.06
FCD	−0.43	−0.92	−1.44	−1.93	0.06	0.05	0.01
(g) K/Pg boundary layer, Bottaccione, Italy							
GP-15	−0.26	−0.59	−0.93	−1.28	0.06	0.05	0.03
(h) K/Pg boundary layer at Um Sohryngkew, Meghalaya. India							
KT-3	−0.35	−0.78	−1.16	−1.61	0.06	0.03	0.05
KT-bulk	−0.64	−0.94	−1.58	−1.89	−0.16	0.01	−0.16
(i) Poty Quarry drill hole, Brazil							
PO-104	−0.17	−0.97	−1.29	−1.87	0.30	−0.03	0.12
PO-105	−0.03	−0.62	−0.89	−1.36	0.31	0.07	0.13
PO-119	−0.31	−1.15	−1.59	−2.45	0.30	0.08	0.25
(j) Bidart, France							
K/Pg boundary layer	−0.04	−0.34	−0.42	−0.74	−1.12	−0.15	0.03
BI-9.28.5	−0.11	−0.57	−0.66	−1.44	−1.56	0.25	0.15
BI-9.34.2	0.05	−0.11	−0.13	−0.31	−0.73	0.12	0.04
BI-9.36.2	0.08	−0.10	−0.07	−0.25	−0.61	0.15	0.03
BI-10.35.1	−0.33	−1.28	−1.68	−2.66	−4.30	0.33	0.06
BI-11.7.3	0.13	−0.16	−0.04	−0.66	−0.73	0.30	0.17

References

Adatte, T., Keller, G., Schoene, B., Samperton, K.M., Font, E., Sial, A.N., Lacerda, L.D., Punekar, J., Fantasia, A., Khadri, S., 2015. Paleoenvironmental influence of Deccan volcanismrelative to the KT extinction. Baltimore. Geological Societyof America Abstracts with Programs 47 (7), 210.

Algeo, T.J., Twitchett, R.J., 2010. Anomalous Early Triassic sediment fluxes due to elevated weathering rates and their biological consequences. Geology 38, 1023–1026.

Algeo, T.J., Hanningan, R., Rowe, H., Brookfield, M., Baud, A., Krystyn, L., Ellwood, B.B., 2007. Sequencing events across the Permain–Triassic boundary, Guryul Ravine

(Kashmir, India). Palaeogeogr. Palaeoclimatol. Palaeoecol. 252, 328–346.
Archbold, N.W., 2000. Palaeobiology of the Australasian Permian. Association of Australasian Palaeontologists Memoir 23, 287–310.
Basu, A.R., Petaev, M.I., Poreda, R.J., Jacobsen, S.B., Becker, L., 2003. Chondritic meteorite fragments associated with the Permian–Triassic boundary in Antarctica. Science 302, 1388–1392.
Baud, A., Margaritz, M., Holser, W.T., 1989. Permian–Triassic of the Tethys: carbon isotope studies. Geol. Rundsch. 78, 649–677.
Becker, L., Poreda, R., Basu, A., Pope, K.O., Harrison, T.M., Nicholson, C., Lasky, R., 2004. Bedout: a possible end-Permian impact crater offshore of Northwestern Australia. Science 304 (5676), 1469–1476. https://doi.org/10.1126/science.1093925.
Benton, M.J., 2003. When Life Nearly Died – The Greatest Mass Extinction of all Time. Thames & Hudson, London (352 pp.).
Benton, M.J., Newell, A.J., 2014. Impacts of global warming on Permo-Triassic terrestrial ecosystems. Gondwana Res. 25, 1308–1337.
Bergquist, B.A., Blum, J.D., 2007. Mass-dependent and-independent fractionation of Hg isotopes by photo reduction in aquatic systems. Science 318, 417–420.
Bergquist, B.A., Blum, J.D., 2009. The odds and evens of mercury isotopes: applications of mass-dependent and mass-independent isotope fractionation. Elements 5, 353–357.
Blum, J.D., Bergquist, B.A., 2007. Reporting of variations in the natural isotopic composition of mercury. Anal. Bioanal. Chem. 388, 353–359.
Blum, J.D., Sherman, L.S., Johnson, M.W., 2014. Mercury isotopes in earth and environmental sciences. Annual Reviews of Earth Planetary Sciences 42, 249–269.
Bond, D.P.G., Grasby, S.E., 2017. On the causes of mass extinctions. Palaeogeogr. Palaeoclimatol. Palaeoecol. 478, 3–29.
Bond, D.P., Wignall, P.B., 2014. Large igneous provinces and mass extinctions: an update. Volcanism, impacts, and mass extinctions: causes and effects. 505, 29–55.
Bosellini, A., 1964. Stratigrafia, petrografia e sedimentologia dele facies carbonatiche al limite Permiano–Trias nelle Dolomiti occidentali. In: Memorie del Museo di Storia Naturale dela Venezia Tridentina 1964–65. XV. Fase. II, pp. 106.
Brand, U., Posenato, R., Came, R., Affek, A., Angiolini, L., Azmy, A., Farabegoli, E., 2012. The end-Permian mass extinction: a rapid volcanic CO_2 and CH_4-climatic catastrophe. Chem. Geol. 322/323, 121–144.
Brand, U., Blamey, N., Garbelli, C., Griesshaber, E., Posenato, R., Angiolini, L., Azmy, K., Farabegoli, E., Came, R., 2016. Methane Hydrate: killer cause of Earth's greatest mass extinction. Palaeoworld 25, 496–507.
Brandner, R., Horacek, M., Keim, L., Scholger, R., 2009. The Pufels/Bulla road section: Deciphering environmental changes across the Permian–Triassic boundary to the Olenekian by integrated litho-, magneto- and isotope stratigraphy. A field trip guide. Geo. Alp 6, 116–132.
Burger, B.J., Estrada, M.V., Gustin, M.S., 2019. What caused Earth's largest mass extinction event? New evidence from the Permian–Triassic boundary in northeastern Utah. Glob. Planet. Chang. 177, 81–100.
Burgess, S.D., Bowring, S.A., 2015. High-precision geochronology confirms volumi-nous magmatism before, during, and after Earth's most severe extinction. Sci. Adv. 1 (7), e1500470. https://doi.org/10.1126/sciadv.1500470.
Burgess, S.D., Bowring, S.A., Shen, S.Z., 2014. High-precision timeline for Earth's most severe extinction. Proceedings of the National Academy of Science, USA 111, 3316–3321.
Burgess, S.D., Muirhead, J.D., Bowring, S.A., 2017. Initial pulse of Siberian Traps sills as the trigger of the end-Permian mass extinction. Nat. Commun. 8, 164.
Cao, C.Q., Zheng, Q.F., 2007. High-resolution lithostratigraphy of the Changhsingian Stage in Meishan section D, Zhejiang. J. Stratigr. 31, 14–22.
Cao, C.Q., Zheng, Q.F., 2009. Geological event sequences of the Permian–Triassic transition recorded in the microfacies in Meishan section. Sci. China Ser. D Earth Sci. 52 (10), 1529–1536.
Cao, C., Wang, W., Jin, Y., 2002. Carbon isotope excursions across the Permian–Triassic boundary in the Meishan section, Zhejiang Province, China. Chin. Sci. Bull. 47, 1125–1129.
Chandler, D.L., 2014. Ancient Whodunit May Be Solved: The Microbes Did it!. MIT News Office. MIT News (March 14). Massachusetts Institute of Technology.
Charbonnier, G., Morales, C., Duchamp-Alphonse, S., Westermann, S., Adatte, T., Föllmi, K.B., 2017. Mercury enrichment indicates volcanic triggering of Valanginian environmental change. Sci. Rep. https://doi.org/10.1038/srep40808. January 2017.
Chen, Z.-Q., Benton, M.J., 2012. The timing and pattern of biotic recovery following the end-Permian mass extinction. Nat. Geosci. 5, 375–383.
Chen, J.-B., Hintelmann, H., Dimock, B., 2010. Chromatographic pre-concentration of Hg from dilute aqueous solutions for isotopic measurement by MC-ICP-MS. J. Anal. At. Spectrom. 25, 1402–1409.
Chen, J.-B., Hintelmann, H., Feng, X.-B., Dimock, B., 2012. Unusual fractionation of both odd and even mercury isotopes in precipitation from Peterborough, ON, Canada. Geochim. Cosmochim. Acta 90, 33–46.
Chen, Z.-Q., Yang, H., Luo, M., Benton, J.J., Kaiho, K., Zhao, L., Huang, Y., Zhang, K., Fang, Y., Jiang, H., Qiu, H., Li, Y., Tu, C., Shi, L., Zhang, L., Feng, X., Chen, L., 2015. Complete biotic and sedimentary records of the Permian–Triassic transition from Meishan section, South China: ecologically assessing mass extinction and its aftermath. Earth Sci. Rev. 149, 67–107.
Cirilli, S., Pirini Radrizzani, C., Ponton, M., Radrizzani, S., 1998. Stratigraphical and palaeoenvironmental analysis of the Permian–Triassic transition in the Badia Valley (Southern Alps, Italy). Palaeogeogr. Palaeoclimatol. Palaeoecol. 138, 85–113.
Clarkson, M.O., Kasemann, S.A., Wood, R.A., Lenton, T.M., Daines, S.J., Richoz, S., Ohnemueller, F., Meixner, A., Poulton, S.W., Tipper, E.T., 2015. Ocean acidifica-tion and the Permo–Triassic mass extinction. Science 34 (8), 229–232.
Coffin, M.F., Gahagan, L.M., 1995. Ontong Java and Kerguelen Plateaux: cretaceous icelands? J. Geol. Soc. Lond. 152, 1047–1052.
Courtillot, V., 1994. Mass extinctions in the last 300 million years: one impact and seven flood basalts? Isr. J. Earth Sci. 43, 255–266.
Courtillot, V.E., Renne, P.R., 2003. On the ages of flood basalt events. C. R. Geosci. 335 (1), 113–140.
Courtillot, V., Jaupart, C., Manighetti, I., Tapponnier, P., Besse, J., 1999. On causal links between flood basalts and continental breakup. Earth Planetary Science Letters 166, 177–195.
Dolenec, T., Buser, S., Dolenec, M., 1999. The Permian–Triassic boundary in the Karavanke Mountains (Slovenia): stable isotope variations in the boundary carbonate rocks of the Kosutnik Creek and Brsnina section. Geologija 41, 17–27.
Dolenec, T., Lojen, S., Ramovš, A., 2001. The Permian–Triassic boundary in Western Slovenia (Idrijca Valley section): magnetostratigraphy, stable isotopes and elemental variations. Chem. Geol. 175, 175–190.
Erwin, D.H., 2003. Impact at the Permo–Triassic boundary: a critical evaluation. Astrobiology 3, 67–74.
Erwin, D.H., 2006. Extinction: How Life on Earth Nearly Ended 250 Million Years Ago. Princeton University Press, New Jersey (296 pages).
Erwin, D.H., Bowring, S.A., Yugan, J., 2002. End-Permian mass extinctions: a review. In: Koeberl, C., MacLeod, K.G. (Eds.), Catastrophic Events and Mass Extinctions: Impacts and Beyond. Geological Society of America Special Paper 356. pp. 363–383.
Faggetter, L.E., Wignall, P.B., Pruss, S.B., Jones, D.S., Grasby, S., Widdowson, M., Newton, R.J., 2019. Mercury chemostratigraphy across the Cambrian Series 2–Series 3 boundary: evidence for increased volcanic activity coincident with extinction? Chem. Geol. 510, 188–199.
Fio, K., Spangenberg, J.E., Vlahović, I., Sremac, J., Velić, I., Mrinjek, E., 2010. Stable isotope and trace element stratigraphy across the Permian–Triassic transition: a redefinition of the boundary in the Velebit Mountain, Croatia. Chem. Geol. 278, 38–57.
Fio, K., Sremac, J., Vlahović, I., Velić, I., Spangenberg, J.E., 2013. Permian deposits and the Permian–Triassic boundary in Croatia: palaeoclimatic implications based on paleontological and geochemical data. Geological Society London, Special Publications 376, 539–548.
Font, E., Adatte, T., Sial, A.N., Lacerda, L.D., Keller, G., Punekar, J., 2016. Mercury anomaly, Deccan Volcanism and the end-Cretaceous Mass Extinction. Geology 44, 171–174.
Foucher, D., Ogrinc, N., Hintelmann, H., 2009. Tracing mercury contamination from the Idrija mining region (Slovenia) to the Gulf of Trieste using Hg isotope ratio measurements. Environmental Science & Technology 43, 33–39.
Ghaderi, A., Leda, L., Schobben, M., Korn, D., Ashouri, A.R., 2014. High-resolution stratigraphy of the Changhsingian (Late Permian) successions of NW Iran and the Transcaucasus based on lithological features, conodonts and ammonoids. Fossil Record 17, 41–57.
Glikson, A., 2004. Bedout: a possible end-Permian impact crater offshore of Northwestern Australia. Science 306, 613. https://doi.org/10.1126/science.1100404.
Gong, Q., Wang, X., Zhao, L., Grasby, S.E., Chen, Z.-Q., Zhang, L., Li, Y., Cao, L., Li, Z., 2017. Mercury spikes suggest volcanic driver of the Ordovician–Silurian mass extinction. Sci. Rep. 7, 5304.
Grasby, S.E., Sanei, H., Beauchamp, B., Chen, Z., 2013. Mercury deposition through the Permo–Triassic biotic crisis. Chem. Geol. 351, 209–216.
Grasby, S.E., Beauchamp, B., Bond, D.P.G., Wignall, P.B., Sanei, 2015a. Mercury anomalies associated with three extinction events (Capitanian crisis, latest Permian extinction and the Smithian/Spathian extinction) in NW Pangea. In: Geological Magazine, https://doi.org/10.1017/S0016756815000436.
Grasby, S.E., Beauchamp, B., Bond, D.P.G., Wignall, P., Talavera, C., Galloway, J.M., Piepjohn, K., Reinhardt, L., Blomeier, D., 2015b. Progressive environmental deterioration in northwestern Pangea leading to the latest Permian extinction. Geol. Soc. Am. Bull. 127, 1311–1347.
Grasby, S.E., Shen, W., Yin, R., Gleason, J.D., Blum, J.D., Lepak, R.F., Hurley, J.P., Beauchamp, B., 2017. Isotopic signatures of mercury contamination in latest Permian oceans. Geology 45, 55–58.
Grasby, S.E., Them II, T.R., Chen, Z., Yin, R., Ardakani, O.H., 2019. Mercury as a proxy for volcanic emissions in the geologic record. Earth-Sci. Rev. 196. https://doi.org/10.1016/j.earscirev.2019.102880.
Grice, K., Cao, C., Love, G.D., Bottcher, M.E., Twitchett, R.J., Grosjean, E., Summons, R.E., Turgeon, S.C., Dunning, W., Jin, W., 2005. Photic zone euxinia during the Permian Triassic superanoxic event. Science 307, 706–709.
Huang, Q., Liu, Y.-L., Chen, J.-B., Feng, X.-B., Huang, W.-L., Yuan, S.-L., Cai, H.-M., Fu, X.-W., 2015. An improved dual-stage protocol to pre-concentrate mercury from airborne particles for precise isotopic measurement. J. Anal. At. Spectrom. 30, 957–966.
Isozaki, Y., 1997. Permo–Triassic boundary superanoxia and stratified superocean: records from lost deep sea. Science 276, 235–238.
Jin, Y.G., Wang, Y., Wang, W., Shang, Q.H., Cao, C.Q., Erwin, D.H., 2000. Pattern of marine mass extinction near the Permian–Triassic boundary in South China. Science 289, 432–436.
Jiskra, M., Wiederhold, J.G., Bourdon, B., Kretzschmar, R., 2012. Solution and speciation controls of mercury isotope fractionation of Hg (II) sorption to goethite. Environ. Sci. Technol. 46, 6654–6662.
Jones, D.S., Martini, A.M., Fike, A., Kaiho, K., 2017. A volcanic trigger for the Late Ordovician mass extinction? Mercury data from south China and Laurentia. Geology. https://doi.org/10.1130/G38940.1.
Koeberl, C., Farley, K.A., Peucker-Ehrenbrink, B., Sephton, M.A., 2004. Geochemistry of the end-Permian extinction event in Austria and Italy: no evidence for an extraterrestrial component. Geology 32, 1053–1056.
Korte, C., Kozur, H.W., 2010. Carbon-isotope stratigraphy across the Permian–Triassic boundary: a review. J. Asian Earth Sci. 39, 215–235.
Korte, C., Kozur, H.W., Partoazar, H., 2004a. Negative carbon isotope excursion at the Permian/Triassic boundary section at Zal, NW-Iran. Hallesches Jahrbuch Geowissenschaften, Reihe B, Beihefte 18, 69–71.

Korte, C., Kozur, H.W., Mohtat-Aghai, P., 2004b. Dzhulfian to lowermost Triassic $\delta^{13}C$ record at the Permian/Triassic boundary section at Shahreza, Central Iran. Hallesches Jahrbuch fur Geowissenschaften B Beiheft 18, 73–78.
Korte, C., Kozur, H.W., Joachimski, M.M., Strauss, H., Veizer, J.N., Schwark, L., 2004c. Carbon, sulfur, oxygen and strontium isotope records, organic geochemistry and biostratigraphy across the Permian/Triassic boundary in Abadeh, Iran. Int. J. Earth Sci. 93, 565–581.
Korte, C., Pande, P., Kalia, P., Kozur, H.W., Joachimski, M.M., Oberhänsli, H., 2010. Massive volcanism at the Permian–Triassic boundary and its impact on the isotopic composition of the ocean and atmosphere. J. Asian Earth Sci. 37, 293–311.
Korte, C., Ruh, M., Palfy, J., Ullmann, C.V., Hesselbo, S.P., 2019. Chemostratigraphy across the Triassic–Jurassic boundary. In: Sial, A.N., Gaucher, C., Ramkumar, M., Ferreira, V.P. (Eds.), Chemostratigraphy Across Major Chronological Boundaries, AGU/Geophysical Monograph. 240. John Wiley & Sons, Inc., pp. 185–210.
Kozur, H.W., 2004. Pelagic uppermost Permian and the Permian–Triassic boundary conodonts of Iran, part I: taxonomy. Hallesches Jahrbuch fur GeowissenschaftenB Beiheft 18, 39–68.
Kozur, H.W., 2005. Pelagic uppermost Permian and the Permian–Triassic boundary conodonts of Iran. Part II: investigated sections and evaluation of the conodont faunas. Hallesches Jahrbuch fur Geowissenschaften B Beiheft 19, 49–86.
Kozur, H.W., 2007. Biostratigraphy and event stratigraphy in Iran around the Permian–Triassic boundary (PTB): implications for the causes of the PTB biotic crisis. Glob. Planet. Chang. 55, 155–176.
Kozur, H.W., Weems, R.E., 2010. The biostratigraphic importance of conchostracans in the continental Triassic of the northern hemisphere. In: Lucas, S.G. (Ed.), The Triassic timescale. 334. Geological Society, London, pp. 315–417 (special publication).
Kozur, H.W., Mostler, H., Rahimi-Yazd, A., 1975. Beitrage zur Mikropalontologie permotriadischer Schichtfolgen. Teil II: Neue Conodonten aus dem Oberperm und der basalen Trias von Nord- und Zentraliran. Geol Palont Mitt Innsbruck 5 (3), 1–23.
Kozur, H.W., Leven, E.J., Lozovskij, V.R., Pjatakova, M.V., 1978. Rasclenenie po konodontam pogranicnych sloev permi i triasa Zakavkazja. Bjul MOIP, otd geol 1978 (5), 15–24.
Kraus, S.H., Brandner, R., Heubeck, C., Kozur, H.W., Struck, U., Korte, C., 2013. Carbon isotope signatures of latest Permian marine successions of the Southern Alps suggest a continental runoff pulse enriched in land plant material. Fossil Record 16 (2013), 97–109.
Kravchinsky, V.A., 2012. Paleozoic large igneous provinces of Northern Eurasia: correlation with mass extinction events. Glob. Planet. Chang. 86–87, 31–36.
Kump, L.R., Arthur, M.A., 1999. Interpreting carbon-isotope excursions: carbonates and organic matter. Chem. Geol. 161, 181–198.
Kwon, H., Kim, G.M., Yong Il, L., 2019. Mercury evidence from the Sino-Korean 1 block for Emeishan volcanism during the Capitanian mass extinction. Geol. Mag. 156, 1105–1110.
Lana, C., Souza Filho, C.R.S., Marangoni, Y.R., Yokoyama, E., Trindade, R.I.F., Tohver, E., Reimold, W.U., 2008. Structural evolution of the 40 km wide Araguainha impact structure, central Brazil. Meteorit. Planet. Sci. 43, 701–716.
Lavric, J.V., Spangenberg, J.E., 2003. Stable isotope (C, O, S) systematics of the mercury mineralization at Idrija, Slovenia: constraints on fluid source and alteration processes. Mineral. Deposita 38, 886–899. https://doi.org/10.1007/s00126-003-0377-9.
Li, R., Jones, B., 2017. Diagenetic overprint on negative $\delta^{13}C$ excursions across the Permian/Triassic boundary: a case study from Meishan section, China. Palaeogeogr. Palaeoclimatol. Palaeoecol. 468, 18–33.
Liu, X.-C., Wang, W., Shen, X.-Z., Gorgij, M.N., Ye, F.C., Zhang, Y.C., Furuyama, S., Kano, A., Chen, X.-Z., 2013. Late Guadalupian to Lopingian (Permian) carbon and strontium isotopic chemostratigraphy in the Abadeh section, central Iran. Gondwana Res. 24 (1), 222–232.
Mei, S., Zhang, K., Wardlaw, B.R., 1998. A refined succession of Changhsingian and Griesbachian neogondolellid conodonts from the Meishan section, candidate of the Global Stratotype Section and Point of the Permian–Triassic boundary. Palaeogeogr. Palaeoclimatol. Palaeoecol. 143, 213–226.
Meyer, K.W., Petersen, S.V., Lohmann, K.C., Blum, J.D., Washburn, S.J., Johnson, M.W., Gleason, J.D., Kurz, A.Y., Winkelstern, I.Z., 2019. Biogenic carbonate mercury and marine temperature records reveal global influence of Late Cretaceous Deccan Traps. Nat. Commun. https://doi.org/10.1038/s41467-019-13366-0https://doi.org/10.
Nascimento-Silva, V.M., Sial, A.N., Ferreira, V.P., Neumann, V.H., Barbosa, J.A., Pimentel, M.M., Lacerda, L.D., 2011. Cretaceous–Paleogene transition at the Paraíba Basin, northeastern, Brazil: carbon-Isotope and mercury subsurface stratigraphies. J. S. Am. Earth Sci. 32, 379–392.
Nascimento-Silva, M.V., Sial, A.N., Ferreira, V.P., Barbosa, J.A., Neumann, V.H., Pimentel, M.M., Lacerda, L.D., 2013. Carbon Isotopes, rare-earth elements and mercury behavior of Maastrichtian–Danian carbonate succession of the Paraíba Basin, northeastern Brazil. In: Bojar, A.V., Melinte-Dobrinescu, M.C., Smit, J. (Eds.), Isotopic Studies in Cretaceous Research. Geological Society, London, Special Publications 382. pp. 85–104.
Ogdena, D.E., Sleep, N.H., 2011. Explosive eruption of coal and basalt and the end-Permian mass extinction. Proceedings of the National Academy of Sciences (PNAS) 109, 59–62.
Payne, J.L., Turchyn, A.V., Paytan, A., DePaolo, D.J., Lehrmann, D.J., Yu, M.Y., Wei, J.Y., 2010. Calcium isotope constraints on the end-Permian mass extinctions. Proceedings of the National Academy of Science USA 107, 8543–8548.
Percival, L.M.E., Witt, M.L.I., Mather, T.A., Hermoso, M., Jenkyns, H.C., Hesselbo, S.P., Al-Suwaidi, A.H., Storm, M.S., Xu, W., Ruhl, M., 2015. Globally enhanced mercury deposition during the end-Pliensbachian extinction and Toarcian OAE: a link to the Karoo–Ferrar Large Igneous Province. Earth Planet. Sci. Lett. 428, 267–280.
Percival, L.M.E., Ruhl, M., Hesselbo, S.P., Jenkyns, H.C., Mather, T.A., Whiteside, J.H., 2017. Mercury evidence for pulsed volcanism during the end-Triassic mass extinction. Proc. Natl. Acad. Sci. 114 (30), 7929–7934.
Percival, L.M.E., Jenkyns, H.C., Mather, T.A., Dickson, A.J., Batenburg, S.J., Ruhl, M., Hesselbo, S.P., Barclay, R., Jarvis, I., Robinson, S.A., Woelders, L., 2018. Does large igneous province volcanism always perturb the mercury cycle? Comparing the records of Oceanic Anoxic Event 2 and the end-Cretaceous to other Mesozoic events. Am. J. Sci. 318, 799–860.
Ramovs, A., 1986. Marine development of the uppermost Zazar beds and the lowermost Scythian beds. In: Permian and Permian–Triassic Boundary in the South Alpine Segment of the Western Tethys. IGCP Project 203, Excursion Guidebook, pp. 39–42.
Rampino, M.R., Prokoph, A., Adler, A., 2000. Tempo of the end-Permian event: high-resolution cyclostratigraphy at the Permian–Triassic boundary. Geology 28, 643–646.
Raup, D.M., Sepkoski Jr., J.J., 1982. Mass extinctions in the marine fossil record. Science 215 (4539), 1501–1503. https://doi.org/10.1126/science.215.4539.1501.
Renne, P., Sprain, C.J., Richards, M.A., Self, S., Vanderkluysen, L., Pande, K., 2015. State shift in Deccan volcanism at the Cretaceous–Paleogene boundary, possibly induced by impact. Science 350, 76–78.
Retallack, G.J., Seyedolali, A., Holser, W.T., Krinsley, D., Krull, E.S., 1998. Shocked quartz at the Permian–Triassic boundary in Australia and Antarctica. Geology 26, 979–982.
Richoz, S., Krystyn, L., Baud, A., Brandner, R., Horacek, M., Mohtat-Aghai, P., 2010. Permian–Triassic boundary interval in the Middle East (Iran and N. Oman): progressive environmental change from detailed carbonate carbon isotope marine curve and sedimentary evolution. J. Asian Earth Sci. 39, 238–253.
Sabatino, N., Ferraro, S., Coccioni, R., Bonsignore, M., Del Core, M., Tancredi, V., Sprovieri, M., 2018. Mercury anomalies in upper Aptian-lower Albian sediments from the Tethys realm. Palaeogeogr. Palaeoclimatol. Palaeoecol. 495, 163–170.
Sahney, S., Benton, M.J., 2008. Recovery from the most profound mass extinction of all time. Proc. R. Soc. B 275 (1636), 759–765.
Sanei, H., Grasby, S.E., Beauchamp, B., 2012. Latest Permian mercury anomalies. Geology 40, 63–66.
Schoene, B., Samperton, K.M., Eddy, M.P., Keller, G., Adatte, T., Bowring, S., Khadri, F.R., Gertsch, B., 2015. U–Pb geochronology of the Deccan Traps and relation to the end-Cretaceous mass extinction. Science 347, 182–184.
Schoene, B., Eddy, M.P., Samperton, K.M., Keller, C.B., Keller, G., Adatte, T., Khadri, S.F., 2019. U-Pb constraints on pulsed eruption of the Deccan Traps across the end-Cretaceous mass extinction. Science 363, 862–866.
Scholle, P.A., Arthur, M.A., 1980. Carbon isotope fluctuations in Cretaceous pelagic limestones: potential stratigraphic and petroleum exploration tool. Am. Assoc. Pet. Geol. Bull. 64, 67–87.
Schwab, V., Spangenberg, J.E., 2004. Organic geochemistry across the Permian–Triassic transition at the Idrijca Valley, Western Slovenia. Appl. Geochem. 19, 55–72.
Sephton, M.A., Looy, C.V., Veefkind, R.J., Brinkhuis, H., de Leeuw, J.W., Visscher, H., 2002. Synchronous record of $\delta^{13}C$ shifts in the oceans and atmosphere at the end of the Permian. In: Koeberl, C., MacLeod, K.G. (Eds.), Catastrophic Events and Mass Extinctions: Impacts and Beyond. Geological Society of America Special Paper 356. pp. 455–462.
Shen, S.Z., Bowring, S.A., 2014. The end-Permian mass extinction: a still unexplained catastrophe. Natl. Sci. Rev. 1, 492–495.
Shen, S.Z., Crowley, J.L., Wang, Y., Bowring, S.A., Erwin, D.H., Sadler, P.M., Cao, C.Q., Rothman, D.H., Henderson, C.M., Ramezani, J., Zhang, H., Shen, Y., Wang, X.D., Wang, W., Mu, L., Li, W.Z., Tang, Y.G., Liu, X.L., Liu, L.J., Zeng, Y., Jiang, Y.F., Jin, Y.G., 2011. Calibrating the end-Permian mass extinction. Science 334, 1367–1372.
Shen, J., Feng, Q., Algeo, T.J., Li, C., Planavsky, N.J., Zhou, L., Zhang, M., 2016. Two pulses of oceanic environmental disturbance during the Permian–Triassic boundary crisis. Earth Planetary Science Letters 443, 139–152.
Shen, S.Z., Ramezani, J., Chen, J., Cao, C.-Q., Erwin, D.H., Zhang, H., Xiang, L., Schoepfer, S.D., Henderson, C.M., Zheng, Q.-F., Bowring, S.A., Wang, Y., Li, X.-H., Wang, X.-D., Yuan, D.-X., Zhang, Y.-X., Mu, L., Wang, J., Wu, Y.-S., 2018. A sudden end-Permian mass extinction in South China. Geol. Soc. Am. Bull. https://doi.org/10.1130/B31909.1.
Shen, J., Chen, J., Algeo, T.A., Yuan, S., Feng, Q., Yu, J., Zhou, L., O'Connell, O., Planavsky, N.J., 2019a. Evidence for a prolonged Permian–Triassic extinction interval from global marine mercury records. Nat. Commun. 10, 1563. https://doi.org/10.1038/s41467-019-09620-0.
Shen, J., Yu, J., Chen, J.-B., Algeo, T.J., Xu, G., Feng, Q., Shi, X., Planavsky, N.H., Shu, W., Xie, S., 2019b. Mercury evidence of intense volcanic effects on land during the Permian–Triassic transition. Geology 47, 1117–1121. https://doi.org/10.1130/G46679.1.
Shen, J., Algeo, T.J., Planavsky, N.J., Yu, J., Feng, Q., Song, H., Song, H., Rowe, H., Zhou, L., Chen, J., 2019c. Mercury enrichments provide evidence of Early Triassic volcanism following the end-Permian mass extinction. Earth Sci. Rev. 195, 191–212.
Shen, J., Algeo, T.J., Chen, J.B., Planavsky, N.J., Feng, Q.L., Yu, J.X., Liu, J.L., 2019d. Mercury in marine Ordovician-Silurian boundary sections of South China is sulfide hosted and non-volcanic in origin. Earth Planetary Science Letters 511, 130–140.
Sial, A.N., Gaucher, C., Silva Filho, M.A., Ferreira, V.P., Pimentel, M.M., Lacerda, L.D., Silva Filho, E.V., Cezario, W., 2010. C-, Sr-isotope and Hg chemostratigraphy of Neoproterozoic cap carbonates of the Sergipano Belt, Northeastern Brazil. In: Karhu, J., Sial, A.N., Ferreira, V.P. (Eds.), Precambrian Isotope Stratigraphy. Precambrian Research 182. pp. 351–372 Special Issue.
Sial, A.N., Lacerda, L.D., Ferreira, V.P., Frei, R., Marquillas, R.A., Barbosa, J.A., Gaucher, C., Windmöller, C.C., Pereira, N.S., 2013. Mercury as a proxy for volcanic activity during extreme environmental turnover: the Cretaceous–Paleogene transition. Palaeogeogr. Palaeoclimatol. Palaeoecol. 387, 153–164.
Sial, A.N., Chen, J.-B., Lacerda, L.D., Peralta, S., Gaucher, C., Frei, R., Cirilli, S., Ferreira, V.P., Marquillas, R.A., Barbosa, J.A., Pereira, N.S., Belmino, I.K.C., 2014. High-resolution Hg chemostratigraphy: a contribution to the distinction of chemical fingerprints of the Deccan volcanism and Cretaceous−Paleogene boundary impact event.

Palaeogeogr. Palaeoclimatol. Palaeoecol. 414, 98–115.
Sial, A.N., Chen, J., Lacerda, L.D., Frei, R., Tewari, V.C., Pandit, M.K., Gaucher, C., Ferreira, V.P., Cirilli, S., Peralta, S., Korte, C., Barbosa, J.A., Pereira, N.S., 2016. Mercury enrichment and mercury isotopes in Cretaceous–Paleogene boundary successions: links to volcanism and palaeoenvironmental impacts. Cretac. Res. 66, 60–81.
Sial, A.N., Chen, J., Lacerda, L.D., Frei, R., Tewari, V.C., Pandit, M.K., Gaucher, C., Ferreira, V.P., Cirilli, S., Peralta, S., Korte, C., Barbosa, J.A., Pereira, N.S., 2017. Reply to comments by Sanjay K. Mukhopadhyay, Sucharita Pal, J. P. Shrivastava on the paper by Sial et al. (2016) Mercury enrichments and Hg isotopes in Cretaceous–Paleogene boundary successions: links to volcanism and palaeoenvironmental impacts. Cretaceous Research 66, 60: 45–81. Cretac. Res. 71. https://doi.org/10.1016/j.cretres.2017.03.004.
Sial, A.N., Chen, J., Lacerda, L.D., Frei, R., Higgins, J., Tewari, V.C., Gaucher, C., Ferreira, V.P., Cirilli, S., Peralta, S., Korte, C., Barbosa, J.A., Pereira, N.S., Ramos, D.S., 2019. Chemostratigraphy across the Cretaceous–Paleogene (K/Pg) boundary: testing the impact and volcanism hypotheses. guest editors In: Sial, A.N., Gaucher, C., Ramkumar, M., Ferreira, V.P. (Eds.), Chemostratigraphy across Major Chronological Boundaries. Geophysical Monograph Series 240. John Wiley & Sons, Inc, pp. 223–257.
Smith, C.N., Kesler, S.E., Blum, J.D., Ryutuba, J.J., 2008. Isotope geochemistry of mercury in source rocks, mineral deposits and spring deposits of the California Coast Ranges, USA. Earth Planet. Sci. Lett. 269, 399–407. https://doi.org/10.1016/j.epsl.2008.02.029.
Song, H., Tong, J., Chen, Z.Q., 2009. Two episodes of foraminiferal extinction near the Permian–Triassic boundary at the Meishan section, South China. Aust. J. Earth Sci. 56, 765–773.
Song, H., Wignall, P.B., Tong, J., Yin, H., 2013. Two pulses of extinction during the Permian–Triassic crisis. Nat. Geosci. 6, 52–56.
Sprain, C.J., Renne, P.R., Vanderkluysen, L., Pande, K., Self, S., Mittal, T., 2019. The eruptive tempo of Deccan volcanism in relation to the Cretaceous-Paleogene boundary. Science 363, 866–870.
Stampfli, G.M., Borel, G.D., 2002. A plate tectonic model for the Paleozoic and Mesozoic constrained by dynamic plate boundaries and restored synthetic oceanic isochrons. Earth Planetary Science Letters 196, 17–33.
Stampfli, G.M., Mosar, J., Favre, P., Pillevuit, A., Vannay, J.-C., 2001. Permo-Mesozoic evolution of the western Tethyan realm: the Neotethys/East- Mediterranean connection. In: Ziegler, P.A., Cavazza, W., Robertson, A.H.F., Crasquin-Soleau, S. (Eds.), PeriTethys memoir 6: Peritethyan rift/wrench basins and passive margins. 186. Mém. Museum Nat. Hist. Nat, Paris, pp. 51–108 IGCP 369.
Taraz, H., Golshani, F., Nakazawa, K., Shimizu, D., Bando, Y., Ishii, K., Murata, M., Okimura, Y., Sakagami, S., Nakamura, K., Tokuoka, T., 1981. The Permian and the Lower Triassic systems in Abadeh region, Central Iran. Memoirs of the Faculty of Science, Kyoto University, Series of Geology & Mineralogy 47 (2), 61–133.
Them, T.R., Jagoe, C.H., Caruthers, A.H., Gill, B.C., Grasby, S.E., Gröcke, D.R., Yin, R., Owens, J.D., 2019. Terrestrial sources as the primary delivery mechanism of mercury to the oceans across the Toarcian Oceanic Anoxic Event (Early Jurassic). Earth Planet. Sci. Lett. 507, 62–72.
Thibodeau, A.M., Bergquist, B.A., 2017. Do mercury isotopes record the signature of massive volcanism in marine sedimentary records? Geology 45, 95–96.
Thibodeau, A.M., Ritterbush, K., Yager, J.A., West, A.J., Ibarra, Y., Bottjer, D.J., Berelson, W.M., Bergquist, B.A., Corsetti, F.A., 2016. Mercury anomalies and the timing of biotic recovery following the end-Triassic mass extinction. Nat. Commun. 7, 11147.
Thomas, B.M., Barber, C.J., 2004. A re-evaluation of the hydrocarbon habitat of the northern Perth Basin. APPEA Journal 44, 59–92.
Thomas, B.M., Willink, R.J., Grice, K., Twitchett, R.J., Purcell, R.R., Archbold, N.W., George, A.D., Tye, S., Alexander, R., Foster, C.B., Barber, C.J., 2004. Unique marine Permian–Triassic boundary section from Western Australia. Aust. J. Earth Sci. 51, 423–430.
Tohver, E., Schmieder, M., Lana, C., Mendes, P.S.T., Jourdan, F., Warren, L., Riccomini, C., 2017. End-Permian impactogenic earthquake and tsunami deposits in the intracratonic Parana Basin of Brazil. Geol. Soc. Am. Bull. 130, 1099–1120. https://doi.org/10.1130/B31626.1.
Wang, Cheng-Yuan, Wang, Zhi-hao, 1981. Permian conodont biostratigraphy of China. Geological Society of America Special Paper 187, 227–236.
Wang, K., Geldsetzer, H.H.J., Krouse, H.R., 1994. Permian–Triassic extinction: organic $\delta^{13}C$ evidence from British Columbia, Canada. Geology 22, 580–584.
Wang, Y., Sadler, P.M., Shen, S.Z., Erwin, D.H., Zhang, Y.C., Wang, X.D., Wang, W., Crowley, J.L., Henderson, C.M., 2014. Quantifying the process and abruptness of the end-Permian mass extinction. Paleobiology 40, 113–129.
Wang, X., Cawood, P.A., Zhao, H., Zhao, L., Grasby, S.E., Chen, Z.-Q., Wignall, P.B., Lv, Z., Han, C., 2018. Mercury anomalies across the end Permian mass extinction in South China from shallow ad deep water depositional environments. Earth Planet. Sci. Lett. 496, 159–167.
Wignall, P.B., 2001. Large igneous provinces and mass extinctions. Earth Sci. Rev. 53, 1–33.
Wignall, P.B., Newton, R., 2003. Contrasting deep-water records from the Upper Permian and Lower Triassic of South Tibet and British Columbia: evidence for a diachronous Mass Extinction. Palaios 18, 153–167.
Wignall, P.B., Twitchett, R.J., 1996. Oceanic anoxia and the end-Permian mass extinction. Science 272, 1155–1158.
Wignall, P.B., Twitchett, R.J., 2002. Extent, duration and nature of the Permian–Triassic superanoxic event. In: Koeberl, C., MacLeod, K.G. (Eds.), Catastrophic Events and Mass Extinctions: Impacts and Beyond. Geological Society of America Special Paper 356. pp. 395–413.
Xie, S.C., Pancost, R.D., Yin, H.F., Wang, H.M., Evershed, R.P., 2005. Two episodes of microbial change coupled with Permo/Triassic faunal mass extinction. Nature 434, 494–497.
Yin, H.F., Sweets, W.C., Yang, Z.Y., Dickins, J.M., 1992. Permo–Triassic events in the eastern Tethys–an overview. In: Sweet, W.C. (Ed.), Permo–Triassic Events in the Eastern Tethys: Stratigraphy, Classification, and Relations With the Western Tethys. Cambridge University Press, 978-0-521-54573-0, pp. 1–7.
Yin, H., Zhang, K., Tong, J., Yang, Z., Wu, S., 2001. The Global Stratotype Section and Point (GSSP) of the Permian–Triassic boundary. Episodes 24, 102–114.
Zhang, F., Romaniello, S.J., Algeo, T.J., Lau, K.V., Clapham, M.E., Richoz, S., Herrmann, A.D., Smith, H., Horacek, M., Anbar, A.D., 2018. Multiple episodes of extensive marine anoxia linked to global warming and continental weathering following the latest Permian mass extinction. Sci. Adv./Research Article 4.
Zheng, Q.F., Cao, C.Q., Zhang, M.Y., 2013. Sedimentary features of the Permian-Triassic boundary sequence of the Meishan section in Changxing County, Zhejiang Province. Sci. China Earth Sci. 56, 956–969.